

THE MILLENNIUM ARECIBO 21-CM ABSORPTION LINE SURVEY. IV.
 STATISTICS OF MAGNETIC FIELD, COLUMN DENSITY, AND
 TURBULENCE
 September 23, 2018

Carl Heiles

Astronomy Department, University of California, Berkeley, CA 94720-3411;
cheiles@astron.berkeley.edu

T.H. Troland

Department of Physics and Astronomy, University of Kentucky, Lexington, KY;
troland@pa.uky.edu

ABSTRACT

We discuss observations of the magnetic field, column density, and turbulence in the Cold Neutral Medium (CNM). The observed quantities are only indirectly related to the intrinsic astronomical ones. We relate the observed and intrinsic quantities by relating their univariate and bivariate probability distribution functions (pdfs). We find that observations of the line-of-sight component of magnetic field do not constrain the pdf of the total field B_{tot} very well, but do constrain the median value of B_{tot} .

In the CNM, we find a well-defined median magnetic field $6.0 \pm 1.8 \mu\text{G}$. The CNM magnetic field dominates thermal motions. Turbulence and magnetism are in approximate equipartition. We find the probability distribution of column density $N_{\perp}(HI)$ in the sheets closely follows $N_{\perp}(HI)^{-1}$ over a range of two orders of magnitude, $0.026 \lesssim N_{\perp}(HI) \lesssim 2.6 \times 10^{20} \text{ cm}^{-2}$. The bivariate distributions are not well enough determined to constrain structural models of CNM sheets.

Contents

1 INTRODUCTION	3
2 SOME IMPORTANT WORDS ON NOTATION	4
3 THEORETICAL CONVERSIONS OF INTRINSIC ASTRONOMICAL PROBABILITY DENSITY FUNCTIONS TO OBSERVED ONES	5
3.1 Conversion of the univariate distributions	6

3.1.1	Conversion of the intrinsic $\phi(\mathbf{B}_{tot})$ to the observed $\psi(\mathbf{B}_{los})$	6
3.1.2	Conversion of the intrinsic $\phi(N_{\perp})$ to the observed $\psi(N_{los})$ for sheets	8
3.1.3	Conversion of the intrinsic $\phi(\mathbf{V}_{turb})$ to the observed $\psi(\mathbf{V}_{turb,los})$ for turbulence perpendicular to \mathbf{B}_{tot}	9
3.2	Conversion of the intrinsic bivariate distribution $\phi(\mathbf{B}_{tot}, N_{\perp})$ to the observed $\psi(\mathbf{B}_{los}, N_{los})$	11
3.2.1	Case of \mathbf{B}_{tot} perpendicular to the sheet	11
3.2.2	Case of \mathbf{B}_{tot} parallel to the sheet	13
3.2.3	Discussion of Figure 2	13
3.3	Conversion of the intrinsic to observed bivariate distributions involving turbulent velocity	14
3.3.1	Conversion of the intrinsic $\phi(\mathbf{B}_{tot}, \mathbf{V}_{turb})$ to the observed $\psi(\mathbf{B}_{los}, \mathbf{V}_{turb,los})$	14
3.3.2	Conversion of the intrinsic $\phi(N_{\perp}, \mathbf{V}_{turb})$ to the observed $\psi(N_{los}, \mathbf{V}_{turb,los})$ for the perpendicular model	14
3.3.3	Conversion of the intrinsic $\phi(N_{\perp}, \mathbf{V}_{turb})$ to the observed $\phi(N_{los}, \mathbf{V}_{turb,los})$ for the parallel model	15
3.3.4	Summary	15
4	DERIVATION OF INTRINSIC ASTRONOMICAL UNIVARIATE PDFs FROM OBSERVED HISTOGRAMS	15
4.1	Derivation of the intrinsic $\phi(\mathbf{B}_{tot})$ from the histogram of observed \mathbf{B}_{obs}	15
4.1.1	Monte Carlo Method	18
4.1.2	A Single Uncertainty δB_{noise} for Purposes of Convolution	19
4.2	Derivation of the intrinsic $\phi(N_{\perp})$ from the histogram of observed N_{los}	20
4.2.1	A Preliminary: latitude dependence of N_{\perp}	20
4.2.2	Derivation of $\phi(N_{\perp})$ assuming the sheets are randomly oriented	22
4.3	Derivation of the intrinsic $\phi(\mathbf{V}_{turb})$ from the histogram of observed $\mathbf{V}_{turb,los}$	25
5	DERIVATION OF PREDICTED BIVARIATE OBSERVED DISTRIBUTIONS AND COMPARISON WITH DATA	25
5.1	$\phi(\mathbf{B}_{tot}, N_{\perp})$ and $\psi(\mathbf{B}_{obs}, N_{los})$	26

5.1.1	Case of B_{tot} Perpendicular to the Sheet	27
5.1.2	Case of B_{tot} Parallel to the Sheet	27
5.2	$\phi(V_{turb}, B_{tot})$ and $\psi(V_{turb,los}, B_{los})$	30
5.3	$\phi(V_{turb}, N_{\perp})$ and $\psi(V_{turb,los}, N_{los})$	30
6	WHICH SHEET MODEL FITS BETTER?	30
7	ASTROPHYSICAL DISCUSSION: MAGNETIC FIELDS	33
7.1	Observational issues	33
7.2	Astrophysical issues	34
8	ASTROPHYSICAL DISCUSSION: COLUMN DENSITIES	35
9	ASTROPHYSICAL DISCUSSION: TURBULENT VELOCITIES	36
10	FINAL COMMENTS: TURBULENT AND MAGNETIC ENERGY EQUIPAR-	
	TION	39

1. INTRODUCTION

Beginning February 1999 we used the Arecibo telescope¹ to begin a series of Zeeman-splitting measurements of the 21-cm line in absorption against continuum radio sources. Heiles & Troland (2004; Paper III and references therein) discussed technical details of the observing technique and data reduction and presented observational results, including magnetic field measurements. As described in Paper III, our analysis of the data identified Gaussian components in the HI absorption spectra. We assume that each component samples a single, isothermal, sheet-like region of CNM. For 69 such components, we are able to estimate (1) the line-of-sight magnetic field strength B_{los} , often subject to significant error, (2) the line-of-sight column density $N(HI)_{los}$, and (3) the contribution of turbulence $V_{turb,los}$ to the line-of-sight velocity dispersion. Systematic instrumental errors are small and the uncertainties are Gaussian distributed. Therefore, our survey has yielded a statistically well-defined ensemble of observed values for each of these three CNM quantities.

From these data, we seek to answer several astrophysically significant questions. For example,

¹The Arecibo Observatory is part of the National Astronomy and Ionosphere Center, which is operated by Cornell University under a cooperative agreement with the National Science Foundation.

what are the probability distribution functions (pdfs) of magnetic field strengths, column densities and turbulent energies in the CNM? Are any of these quantities statistically related to each other? If so, can we determine if the magnetic field lies preferentially in the planes of CNM sheets or perpendicular to them? What is the ratio of magnetic to turbulent energy in the CNM? As we will see below, the data provide answers to some, but not all, of these questions.

We observe quantities that are only indirectly related to the intrinsic astronomical ones. For the magnetic field, we observe the line of sight component B_{los} , not the total field B_{tot} . For the column density $N(HI)$, we must account for the fact that the Cold Neutral Medium is in sheets, not spheres; our observed column densities N_{los} are always larger than the intrinsic column density normal to the sheet N_{\perp} . To properly interpret our results and to address the questions listed above, we must consider how the intrinsic and observed quantities are related in a statistical sample. These statistical transformations, and the results of applying them to our data, are the focus of the current paper.

We treat both univariate distributions and bivariate distributions. The univariate distributions are most interesting because we obtain definitive results; in contrast, the possible correlations that could be revealed by bivariate distributions are obscured by noise and inadequate numbers of data. Accordingly, the reader who is interested in astrophysical results can concentrate on the sections dealing with univariate distributions of magnetic field, column density, and turbulent velocity. We recommend beginning with §2, which introduces the notation and concepts of intrinsic and observed quantities. We develop the theoretical relationships between observed and intrinsic univariate distributions in §3, and use these to obtain the actual intrinsic univariate distributions in §3.1. Finally, we discuss astrophysical implications in §7, §8, §9, and §10.

2. SOME IMPORTANT WORDS ON NOTATION

We need to introduce important distinguishing nomenclature because of the anisotropic nature of magnetic-field-related quantities. First, we make the crucial distinction between *line-of-sight (los)* quantities, such as B_{los} , and the *intrinsic astronomical* ones such as B_{tot} . We will often refer to the latter with one the shorter terms “intrinsic” or “astronomical”. The important point is to distinguish between observed and intrinsic quantities.

The line-of-sight component is the quantity to which the telescope responds, and we designate these with the subscript *los*. There is an additional complication for the magnetic field, which is the presence of significant instrumental noise. Thus, we must distinguish between the line-of-sight component of the field, designated by B_{los} , and the actual measured value, designated by B_{obs} . We define

$$B_{los} \equiv \text{the line-of-sight component of } B_{tot} ; \quad (1a)$$

$$B_{obs} \equiv \text{the observed field strength .} \quad (1b)$$

The essential difference between B_{los} and B_{obs} is

$$B_{obs} = B_{los} + \delta B_{noise} \quad (1c)$$

where δB_{noise} is the uncertainty contributed by random measurement noise.

Noise is small enough to neglect for column density and velocity, so the observed quantities are essentially identical to the *los* ones; we will use the subscript *los* for the observed quantities, with the implicit assumption that their uncertainties from noise are negligible. For column density, we always refer to HI so we often write N instead of $N(HI)$. We usually consider sheets, for which the column density perpendicular to the face is $N(HI)_{\perp}$ and for which the apparent column density along the line of sight is

$$N_{los} \equiv N(HI)_{los} = N(HI)_{obs} = \frac{N(HI)_{\perp}}{\cos \theta} , \quad (2)$$

where θ is the angle between the sheet's normal vector and the line of sight. Similarly, for velocity linewidths, we use the symbol $V_{turb,los}$ to indicate the line-of-sight component of the turbulent velocity.

Finally, the probability density functions (pdf) of intrinsic quantities, such as B_{tot} , differ from those of the line-of-sight quantities. We will always use the symbol ϕ for the pdfs of intrinsic quantities, and the symbol ψ for line-of-sight (*los*) or the observed ones. Unless otherwise specified, units are always as follows: magnetic field B in μ Gauss; column density N in HI atoms 10^{20} cm^{-2} ; velocity V in km s^{-1} .

3. THEORETICAL CONVERSIONS OF INTRINSIC ASTRONOMICAL PROBABILITY DENSITY FUNCTIONS TO OBSERVED ONES

We begin with some light theory by considering elementary transformations of magnetic field and column density in statistical distributions. First, we consider how the intrinsic probability density function (pdf) of B_{tot} , defined as $\phi(B_{tot})$, converts to the observed histogram or pdf of observed B_{los} , defined as $\psi(B_{los})$, under the assumption that fields are randomly oriented with respect to the observer. Note the important distinction: B_{tot} is the total field strength; B_{los} is the observed line-of-sight component, which is always smaller.

Next we incorporate one of the fundamental results of Heiles & Troland (2003; Paper II), namely that the CNM components are thin sheets. We define $N_{\perp} = N(HI)_{\perp}$ as the HI column density perpendicular to the sheet; the observed quantity is $N_{los} = N(HI)_{los}$, which is always larger. As with the magnetic field, we consider how the pdf $\phi(N_{\perp})$ converts to the observed histogram or pdf $\psi(N_{los})$, again under the assumption that the sheets are randomly oriented with respect

to the observer. We also consider the statistical transformation of the distribution of the actual nonthermal velocity dispersion V_{turb} to that of the observed one $V_{turb,los}$ under the assumption that turbulence is perpendicular to the magnetic field.

We then tackle the bivariate distributions. First we consider how the bivariate distribution $\phi(B_{tot}, N_{\perp})$ converts to the observed one $\psi(B_{los}, N_{los})$. We then assume two extreme models, one with the fields always perpendicular to the sheets and one with fields parallel to the sheets, and assuming random orientations derive the observed bivariate distributions $\psi(B_{los}, N_{los})$ for the two cases. We illustrate and discuss the result by considering delta-function distributions of B_{tot} and N_{\perp} , and we also apply the transformation of the observed $\psi(B_{los}, N_{los})$ to its intrinsic counterpart $\phi(B_{tot}, N_{\perp})$. Finally, we examine the bivariate distributions involving the pairs $(V_{turb,los}, N_{los})$ and $(V_{turb,los}, B_{los})$, which produces little in the way of useful results.

3.1. Conversion of the univariate distributions

3.1.1. Conversion of the intrinsic $\phi(B_{tot})$ to the observed $\psi(B_{los})$

We first consider the simple case in which all clouds have the same B_{tot} , which is randomly oriented with respect to the observer. The line of sight component B_{los} is

$$B_{los} = B_{tot} \cos \theta , \quad (3)$$

where θ is the angle between the field direction and the line of sight. θ can run from 0 to π , but the intervals from 0 to $\frac{\pi}{2}$ and $\frac{\pi}{2}$ to π are identical except for a change of sign in B_{los} . It's simpler and no less general to consider the smaller interval θ from 0 to $\frac{\pi}{2}$ so that we can ignore the slight complications of the sign change. In this case, the pdf of θ is the familiar

$$\phi_{\theta}(\theta) = \sin \theta \quad (4)$$

and we wish to know the pdf of B_{los} , which is given by (see Trumpler and Weaver 1953 for a discussion of these conversions)

$$\psi(B_{los}) = \phi_{\theta}[\theta(B_{los})] \left| \frac{d[\theta(B_{los})]}{dB_{los}} \right| , \quad (5)$$

which gives

$$\psi(B_{los}) = \begin{cases} \frac{1}{B_{tot}} & \text{if } 0 \leq B_{los} \leq B_{tot} \\ 0 & \text{otherwise} \end{cases} \quad (6)$$

In other words, B_{los} is uniformly distributed between the maximum possible extremes 0 and B_{tot} (actually $\pm B_{tot}$). This leads to the well-known results that in a large statistical sample for which a constant B_{tot} is viewed at random angles, both the median and the mean observed field strengths are half the total field strength and that $B_{los}^2 = \frac{B_{tot}^2}{3}$. More generally, observed fields are always smaller than the actual total fields, and with significant probability they range all the way down to zero.

Now suppose B_{tot} has an arbitrary pdf $\phi(B_{tot})$. The univariate pdf $\phi(\theta)$ becomes the bivariate pdf $\phi(B_{tot}, \theta)$, and we assume B_{tot} is independent of the observer's location so that $\phi(B_{tot}, \theta) = \phi_{B_{tot}}(B_{tot})\phi_\theta(\theta)$. Note that we introduce subscripts on the different ϕ 's to distinguish them, instead of designating them with different Greek letters. To obtain $\psi(B_{los})$ we again follow the standard techniques; it's easy to integrate over θ and obtain

$$\psi(B_{los}) = \int_{[B_{los} > B_{tot, \min}]}^{\infty} \frac{\phi(B_{tot})}{B_{tot}} dB_{tot}, \quad (7)$$

where the symbol $[B_{los} > B_{tot, \min}]$ means the larger of the two quantities. The presence of B_{tot} in the denominator means that smaller ranges of B_{los} are emphasized. This is commensurate with the equation 6's uniform pdf for a single field value. We note that this can be regarded as an integral equation for $\phi(B_{tot})$ and it is straightforward to invert.

Figure 1 illustrates the solution of equation 7 for four functional forms of $\phi(B_{tot})$ plotted against $\frac{|B|}{|B_{1/2}|}$, where the subscript 1/2 denotes the median value. These forms include the following:

1. ϕ a Kronecker delta function (DELTA FCN), $\phi_{B_{tot}}(B_{tot}) = \delta(B_{tot} - B_{tot,0})$, yielding ψ a flat function (as discussed immediately above, equation 6);
2. ϕ a flat distribution (FLAT FCN) between $0 \leq |B_{tot}| \leq B_0$, yielding $\psi \propto \ln\left(\frac{B_0}{B_{los}}\right)$;
3. ϕ a weighted Gaussian (EXP FCN),

$$\phi(B_{tot}) = \sqrt{\frac{2}{\pi B_0^2}} \frac{B_{tot}^2}{2B_0^2} e^{-(B_{tot}^2/2B_0^2)}, \quad (8)$$

yielding ψ a Gaussian with dispersion B_0 .

4. ϕ a Gaussian (GAUSS FCN) with dispersion B_0 , yielding $\psi \propto E_1\left(\frac{B_{los}^2}{2B_0^2}\right)$, where E_1 is the exponential integral of order 1.

All four $\phi(B_{tot})$ are plotted with respect to $\frac{B_{tot}}{B_{tot,1/2}}$, so the medians of all lie at unity on the x -axis. However, the means differ. Similarly, the medians and means of the associated $\psi(B_{los})$ differ from each other. These relationships between median and mean are summarized in Table 1.

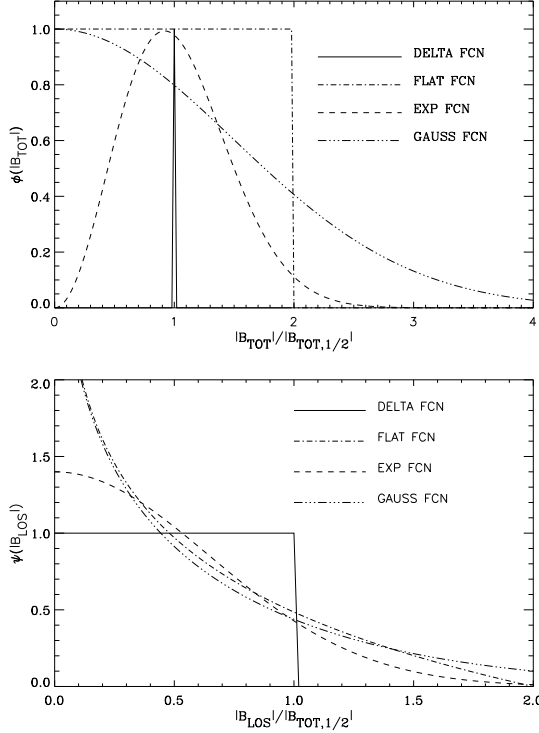


Fig. 1.— Top panel: The intrinsic $\phi(B_{tot})$ for four representative functional forms. Bottom panel: their line-of-sight counterparts $\psi(B_{los})$. The vertical scales are arbitrary.

The medians and means for $\psi(B_{los})$ are all about half those for $\langle B_{tot} \rangle$, which is a direct result of the weighting by B_{tot}^{-1} in equation 7.

Figure 1 is disappointing from the observer’s standpoint, because the observed distributions $\psi(B_{los})$ do not differ very much. These differences become smaller—inconsequential, in fact—when one includes measurement noise, as we shall discuss in detail for our data in §4.1. Unfortunately, given the inevitable errors in *any* observation that is sensitive to B_{los} , it seems practically impossible to distinguish among different functional forms for $\phi(B_{tot})$. Nevertheless, the average value of B_{los} is close to half the average value of B_{tot} for a wide range of intrinsic pdfs of the latter; this also applies to the medians, but less accurately. Therefore, this rule of thumb may be used to estimate the median or average B_{tot} from an ensemble of measurements of B_{los} .

3.1.2. Conversion of the intrinsic $\phi(N_{\perp})$ to the observed $\psi(N_{los})$ for sheets

Here we assume the CNM is distributed in sheets having HI column density N_{\perp} in the direction perpendicular to the sheet. If the normal vector to the sheet is oriented at angle θ with respect to

the line of sight, we have

$$N_{los} = \frac{N_{\perp}}{\cos \theta} . \quad (9)$$

To find $\psi(N_{los})$ we follow the same procedures as above in §3.1.1. For a single value of N_{\perp} we obtain

$$\psi(N_{los}) = \begin{cases} \frac{N_{\perp}}{N_{los}^2} & \text{if } N_{los} \geq N_{\perp} \\ 0 & \text{otherwise} \end{cases} \quad (10)$$

For a single N_{\perp} , N_{los} has a long tail extending to infinity. The median value of N_{los} is $N_{los,1/2} = 2N_{\perp}$, reflecting the increased observed column for tilted sheets. The mean value of N_{los} ($\langle N_{los} \rangle$) is not defined because the integral diverges logarithmically; of course, this doesn't occur in the real world, where sheets don't extend to infinity. For example, if all sheets have aspect ratio 5 : 1, then $\langle N_{los} \rangle = 1.6N_{\perp}$ and $N_{los,1/2} = 1.7N_{\perp}$.

For an arbitrary pdf $\phi(N_{\perp})$ and infinite slabs, we obtain

$$\psi(N_{los}) = \frac{1}{N_{los}^2} \int_0^{[N_{los} < N_{\perp max}]} N_{\perp} \phi(N_{\perp}) dN_{\perp} . \quad (11)$$

As above, this can be regarded as an integral equation for $\phi(N_{\perp})$ and it is almost as straightforward to invert.

3.1.3. Conversion of the intrinsic $\phi(\mathbf{V}_{turb})$ to the observed $\psi(\mathbf{V}_{turb,los})$ for turbulence perpendicular to \mathbf{B}_{tot}

The observed velocity width comes from two sources, thermal and nonthermal. We can separate these because we have independent measurements of the kinetic temperature. Thus, we can derive

Table 1. Medians and Means of B_{tot} and B_{los} for Representative pdfs

$\phi(B_{tot})$	$B_{tot,1/2}$	$\langle B_{tot} \rangle$	$B_{los,1/2}$	$\langle B_{los} \rangle$
DELTA FCN	1.00	1.00	0.50	0.50
FLAT FCN	1.00	1.00	0.40	0.52
GAUSS FCN	1.00	1.18	0.38	0.59
EXP FCN	1.00	1.04	0.44	0.51

the line-of-sight (los) nonthermal (“turbulent”) line width and its associated energy density. How this relates to the total turbulent energy density depends on whether the turbulence is $1d$, $2d$, or $3d$.

Here we assume that this turbulence is $2d$, i.e. we assume that it is restricted to motions perpendicular to the mean magnetic field. We make this assumption because we show below that the typical turbulent Mach number is equal to 3.7. For velocities that are parallel to the magnetic field, such turbulence would produce strong shocks that would damp very rapidly. However, velocities that are perpendicular to the magnetic field can be as high as the Alfvén velocity without producing shocks; this is the basis for considering turbulent motions perpendicular to the mean field. We caution, however, that numerical simulations of magnetohydrodynamical turbulence find that magnetic fields do not ameliorate turbulent dissipation (MacLow et al. 1998), so our assumption might not have any basis in physical reality; in this case the turbulence is isotropic ($3d$) and the observed distribution $\psi(V_{turb,los})$ is equal to the intrinsic one $\phi(V_{turb})$.

Suppose that the magnetic field is oriented at angle θ with respect to the line of sight, as in §3.1.1. Suppose that turbulent motions are perpendicular to the fieldlines and isotropic in the azimuthal directions around the fieldlines, and along one direction perpendicular to B have width V_{turb} ; this makes the full turbulent width $2^{1/2}V_{turb}$. Then line-of-sight width is

$$V_{turb,los} = V_{turb} \sin \theta . \quad (12)$$

To find $\psi(V_{turb,los})$ we again follow the same procedures as in §3.1.1 and obtain

$$\psi(V_{turb,los}) = \begin{cases} \frac{V_{turb,los}}{V_{turb}} \left[V_{turb}^2 - V_{turb,los}^2 \right]^{-1/2} & \text{if } V_{turb,los} < V_{turb} \\ 0 & \text{otherwise} \end{cases} \quad (13)$$

Given a value for V_{turb} , $\psi(V_{turb,los}) \rightarrow \infty$ as $V_{turb} \rightarrow V_{turb,los}$, but the cumulative distribution is well-defined with

$$cum(V_{turb,los}) = 1 - \left[1 - \left(\frac{V_{turb,los}}{V_{turb}} \right)^2 \right]^{1/2} \quad (14)$$

which gives the median $V_{turb,los,1/2} = 0.87V_{turb}$ median and mean $\langle V_{turb,los} \rangle = 0.79V_{turb}$. These high values reflect the large fraction of sheets tilted to the line of sight, where $V_{turb,los}$ is large.

For an arbitrary pdf $\phi(V_{turb})$ we obtain

$$\psi(V_{turb,los}) = \int_{V_{turb,los}}^{\infty} \frac{V_{turb,los}}{V_{turb}} \left[V_{turb}^2 - V_{turb,los}^2 \right]^{-1/2} \phi_{V_{turb}}(V_{turb}) dV_{turb} \quad (15)$$

In contrast to the two cases above, this integral equation is not straightforward to invert. It is a Volterra equation of the first kind and, following the identical example in Trumpler & Weaver (1953), it can be rewritten as Abel integral equation. The analytic solution is

$$\phi(V_{turb}) = -\frac{2V_{turb}^2}{\pi} \frac{d}{dV_{turb}} \int_{V_{turb}}^{\infty} \frac{V_{turb}}{V_{turb,los}^2} [V_{turb,los}^2 - V_{turb}^2]^{-1/2} \psi(V_{turb,los}) dV_{turb,los} \quad (16)$$

3.2. Conversion of the intrinsic bivariate distribution $\phi(B_{tot}, N_{\perp})$ to the observed $\psi(B_{los}, N_{los})$

We have measured both B_{los} and N_{los} and wish to know the bivariate distribution $\psi(B_{los}, N_{los})$. We proceed by first assuming that B_{tot} , N_{\perp} , and of course θ are all uncorrelated. To proceed we consider two different models.

3.2.1. Case of B_{tot} perpendicular to the sheet

We refer to this as the *perpendicular model*. The only angle involved is θ , so that the original pdf is the trivariate $\phi(B_{tot}, N_{\perp}, \theta)$. This case is simplified because only $\cos \theta$ is involved, which makes $B_{los} \propto \frac{1}{N_{los}}$. Converting the original distribution $\phi(B_{tot}, N_{\perp}, \theta)$ to the one involving the observed parameters yields

$$\psi(B_{los}, N_{los}, N_{\perp}) = \frac{1}{N_{los}} \phi_{Btot} \left(\frac{B_{los} N_{los}}{N_{\perp}} \right) \phi_{N_{\perp}}(N_{\perp}) \quad (17)$$

Here we have chosen to eliminate B_{tot} and express the result in terms of N_{\perp} ; we could have gone the other way. To obtain ψ in terms of only the observed quantities, we need to integrate over N_{\perp} , but we cannot do this without knowing $\phi_{N_{\perp}}(N_{\perp})$. Later we use the one obtained from observations.

For now we consider the illustrative case for which all B_{tot} and N_{\perp} are identical, i.e. $\phi_{Btot}(B_{tot}) = \delta(B_{tot} - B_{tot,0})$ and $\phi_{N_{\perp}}(N_{\perp}) = \delta(N_{\perp} - N_{\perp,0})$, where δ is the Kronecker delta function. This is a trivial case because all observed points fall on the line

$$B_{los} = B_{tot,0} \frac{N_{\perp,0}}{N_{los}} \quad (18)$$

which is shown in the top panel of Figure 2.

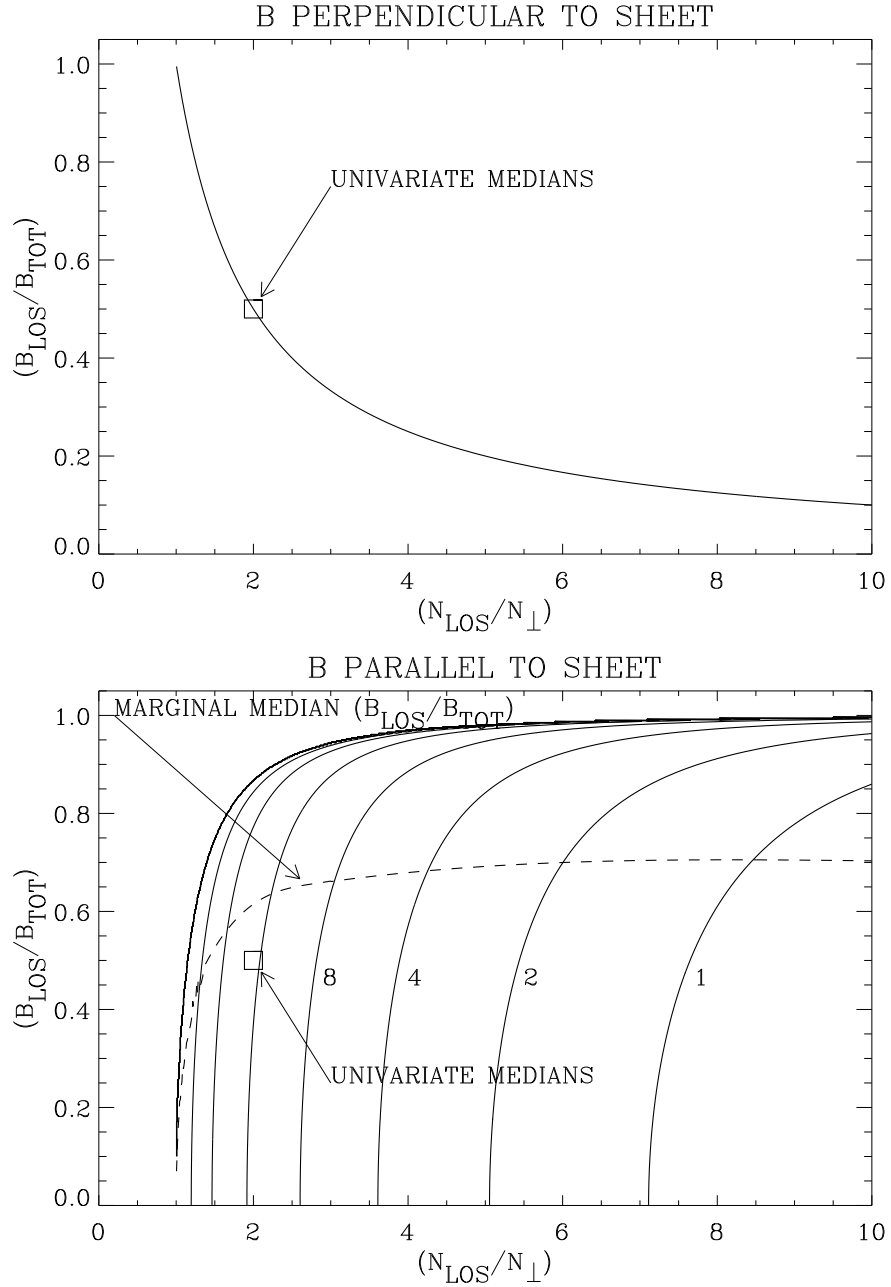


Fig. 2.— The theoretical observed joint pdfs $\psi(B_{\text{los}}, N_{\text{los}})$ for the illustrative case of δ -function distributions for B_{los} and N_{los} . The top panel shows the pdf for B_{tot} perpendicular to the sheets; it degenerates into a single line. The bottom panel is for B_{tot} parallel to the sheets; contours are spaced by factors of 2 with arbitrary scaling, and the dashed line shows the median B_{los} versus N_{los} .

3.2.2. Case of \mathbf{B}_{tot} parallel to the sheet

This case is more complicated because B_{los} depends on two angles. These are θ , which is the tilt of the sheet with respect to the observer, and Φ , which is the azimuthal angle of the field within the sheet. We have $B_{los} = B_{tot} \sin \theta \sin \Phi$. This means the pdf ϕ is quadrivariate. Again we assume everything is uncorrelated and eliminate θ and Φ . Obtaining the observed distribution is somewhat cumbersome but yields the surprisingly straightforward result

$$\psi(B_{los}, N_{los}, B_{tot}, N_{\perp}) = \frac{N_{\perp}}{\pi N_{los}} [(B_{tot} N_{los})^2 - (B_{tot} N_{\perp})^2 - (B_{los} N_{los})^2]^{-1/2} \phi_{B_{tot}}(B_{tot}) \phi_{N_{\perp}}(N_{\perp}) \quad (19)$$

Later we use observed distributions, but for now we again consider the illustrative case of delta functions for B_{tot} and N_{\perp} . Integrating over B_{tot} and N_{\perp} yields

$$\psi(B_{los}, N_{los}) = \frac{N_{\perp 0}}{\pi N_{los}} [(B_{tot,0} N_{los})^2 - (B_{tot,0} N_{\perp 0})^2 - (B_{los} N_{los})^2]^{-1/2} \quad (20)$$

which is illustrated in the bottom panel of Figure 2.

3.2.3. Discussion of Figure 2

Figure 2 exhibits the joint pdfs for the two sheet models (B_{tot} perpendicular and parallel to the sheets—the “perpendicular” and “parallel” models). The median observed column density $N_{los1/2}$ is twice the assumed N_{\perp} and the median observed magnetic $B_{los1/2}$ is half the assumed B_{tot} ; these univariate medians are indicated by squares on the two panels. The significance of these squares is that half the observed B_{los} , and half the observed N_{los} , are smaller and half larger. Finally, the dashed line in the bottom panel exhibits the median $B_{los1/2}$ versus N_{los} ; we calculate this by extracting the conditional pdf $\psi(B_{los}|N_{los})$ versus N_{los} and calculating the median from its cumulative distribution, thus obtaining $B_{los,1/2}$ versus N_{los} .

Figure 2 illustrates a crucial observational signature at large N_{los} that distinguishes between the two sheet models. More specifically, for the perpendicular model, large N_{los} goes with small B_{los} , and *vice-versa* for the parallel model. For the perpendicular model, *all* of the datapoints having N_{los} above its univariate median (indicated by the square) have B_{los} *below* its univariate median. In contrast, for the parallel model *most* (66%) of the datapoints have B_{los} *above* its univariate median: as N_{los} gets large, the conditional pdf $\psi(B_{los}|N_{los}) \rightarrow \frac{N_{\perp 0}}{\pi N_{los}^2} (B_{tot,0}^2 - B_{los}^2)^{-1/2}$, which produces the median $B_{los1/2} \rightarrow 0.71 B_{tot}$.

3.3. Conversion of the intrinsic to observed bivariate distributions involving turbulent velocity

In this section, we derive and display the observed bivariate distributions involving $\psi(B_{los}, V_{turb,los})$ and $\psi(N_{los}, V_{turb,los})$, under the assumption that the turbulent velocity is perpendicular to the magnetic field.

3.3.1. Conversion of the intrinsic $\phi(B_{tot}, V_{turb})$ to the observed $\psi(B_{los}, V_{turb,los})$

The joint pdf $\psi(B_{los}, V_{turb,los})$ is the same for both the parallel and perpendicular models, and indeed does not depend on whether there are sheets or not, because V_{turb} is perpendicular to B_{tot} so that there is a unique relationship $\frac{B_{los}}{B_{tot}} = \left[1 - \left(\frac{V_{turb,los}}{V_{turb}}\right)^2\right]^{1/2}$. As before, we begin with trivariate distributions involving θ , B_{tot} and V_{turb} . We eliminate θ to obtain

$$\psi(B_{los}, V_{turb,los}) = \int_{V_{turb,los}}^{\infty} \frac{V_{turb,los}}{V_{turb}^2} \left[1 - \frac{V_{turb,los}^2}{V_{turb}^2}\right]^{-1/2} \phi_{B_{tot}} \left(B_{los} \left[1 - \frac{V_{turb,los}^2}{V_{turb}^2}\right]^{-1/2}\right) \phi_{V_{turb}}(V_{turb}) dV_{turb} \quad (21)$$

The top panel of Figure 3 displays this joint pdf for delta-function distributions of B_{tot} and V_{turb} . Because we assume that the B_{tot} and V_{turb} are perpendicular, strong fields go with small velocities and *vice-versa*. There are no contours; they all collapse into a line because, for the delta-function distributions, there is a one-to-one relationship between B_{los} and $V_{turb,los}$.

3.3.2. Conversion of the intrinsic $\phi(N_{\perp}, V_{turb})$ to the observed $\psi(N_{los}, V_{turb,los})$ for the perpendicular model

In contrast to the above case, the relation between $\phi(N_{\perp}, V_{turb})$ and $\psi(N_{los}, V_{turb,los})$ does depend on the model. For the model with B_{tot} perpendicular to the sheet we have $N_{los} = \frac{N_{\perp}}{\cos \theta}$ and $V_{turb,los} = V_{turb} \sin \theta$. We obtain

$$\psi(N_{los}, V_{turb,los}) = \int_{N_{los}}^{\infty} \frac{N_{\perp}}{N_{los}^2} \left[1 - \frac{N_{\perp}^2}{N_{los}^2}\right]^{-1/2} \phi_{V_{turb}} \left(V_{turb,los} \left[1 - \frac{N_{\perp}^2}{N_{los}^2}\right]^{-1/2}\right) \phi_{N_{\perp}}(N_{\perp}) dN_{\perp} \quad (22)$$

The middle panel of Figure 3 displays this joint pdf for delta-function distributions of N_{\perp} and V_{turb} . There are no contours; they all collapse into a line because, for the delta-function distributions, there is a one-to-one relationship between B_{los} and $V_{turb,los}$. Because we assume that the B_{tot} and V_{turb} are perpendicular, high HI columns go with small velocities and *vice-versa*.

3.3.3. Conversion of the intrinsic $\phi(N_{\perp}, V_{turb})$ to the observed $\phi(N_{los}, V_{turb,los})$ for the parallel model

The parallel model is more complicated, as it was in §3.2.2, because Φ enters explicitly: because V_{turb} is assumed to be perpendicular to B_{tot} , $V_{turb,los} = V_{turb}[1 - (\sin \theta \sin \Phi)^2]^{1/2}$. The final expression equivalent to 22 is quite complicated, so we deal with it numerically. The bottom panel of Figure 3 displays this joint pdf for delta-function distributions of N_{\perp} and V_{turb} ; the contours come from a Monte-Carlo calculation.

3.3.4. Summary

The complicated nature of the the univariate distribution $\psi(V_{turb,los})$ in equation 15 means that the bivariate distributions that involve $V_{turb,los}$ are even more complicated and preclude closed-form solutions when we use the observationally derived pdfs. However, we can easily present the bivariate results for delta-function distributions of B_{tot} , V_{turb} , and N_{\perp} , shown in Figure 3. Two, $\psi(B_{los}, V_{turb,los})$ and $\psi(N_{los}, V_{turb,los})$, degenerate into lines because the observed variables depend only on θ .

4. DERIVATION OF INTRINSIC ASTRONOMICAL UNIVARIATE PDFs FROM OBSERVED HISTOGRAMS

4.1. Derivation of the intrinsic $\phi(B_{tot})$ from the histogram of observed B_{obs}

Figure 4, top panel, exhibits the histogram of measured field strengths B_{obs} . It contains 69 measurements, of which only 12 have the measurement error $\delta B_{los,m} < 2.5 B_{los,m}$. This histogram is not symmetric: it has 42 instances of $B_{obs} > 0$ and 27 instances of $B_{obs} < 0$. For a randomly distributed angle between line-of-sight and the field direction, one expects the numbers to be equal; the probability that we obtain this imbalance, or worse, is given by integrating the binomial (coin-tossing) pdf and is equal to 0.042. This is fairly low, but is hardly low enough to rule out the random distribution. However, the small probability might indicate that the selection of sources in the Arecibo sky does, in fact, involve non-randomness.

We proceed on the assumption that the distribution of angles is, indeed, random. This allows us to compare the histogram of the absolute value of measured field $|B_{los,m}|$ with the theoretical expectation for various assumed intrinsic pdfs of B_{tot} . Figure 4, bottom panel, exhibits this distribution, but symmetrized so that every entry for a positive B_{obs} is matched by one with negative B_{obs} . The solid line is best fit the Gaussian pdf

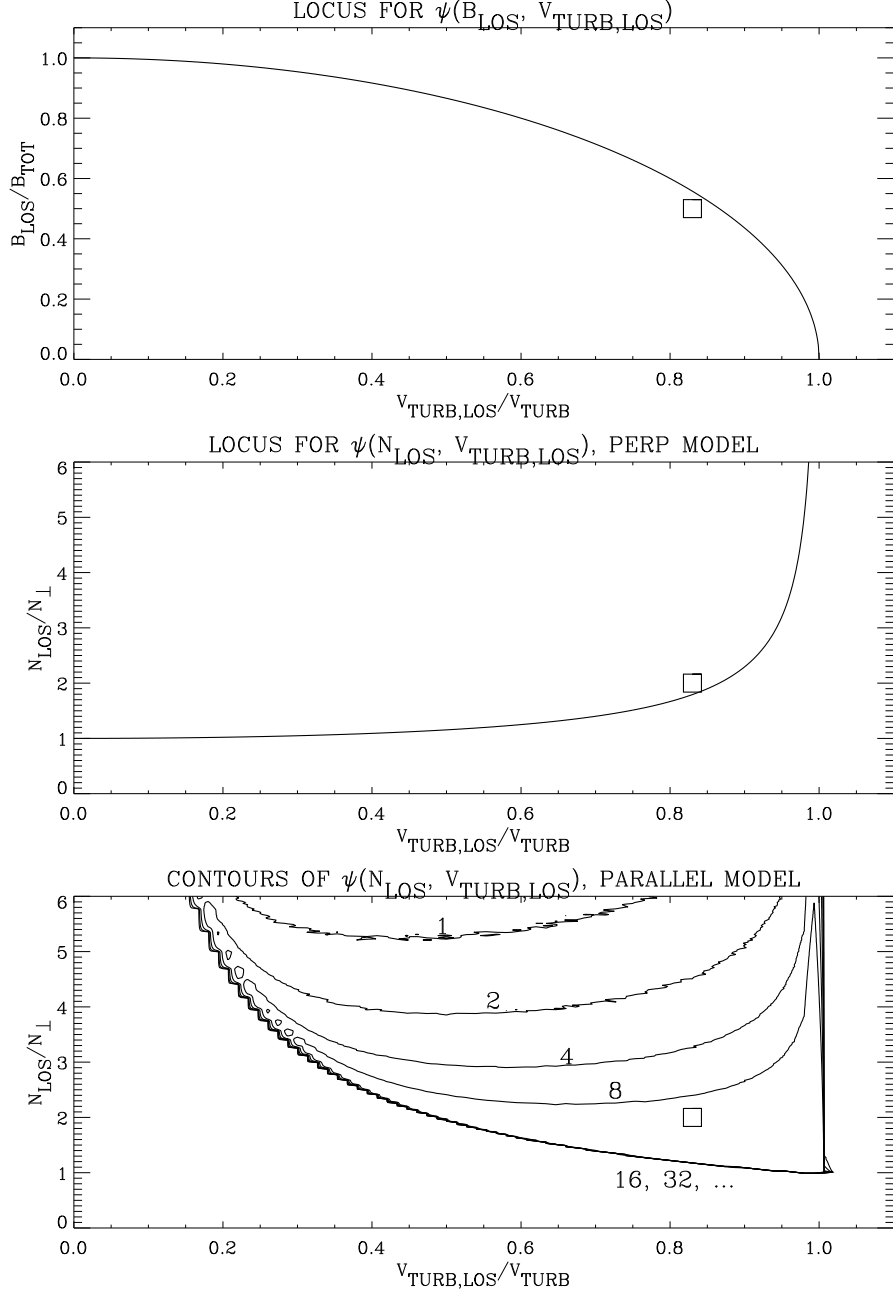


Fig. 3.— Bivariate distributions for the model having turbulent velocities perpendicular to the magnetic field, discussed in §3.3. These distributions assume δ -function distributions of the astronomical parameters V_{turb} , B_{tot} , and N_{\perp} . Top panel, the locus of contours of the bivariate distribution $\psi(B_{los}, V_{turb,los})$ (observed quantities). Middle and bottom panels: contours of $\psi(N_{los}, V_{turb,los})$. Squares show the univariate medians.

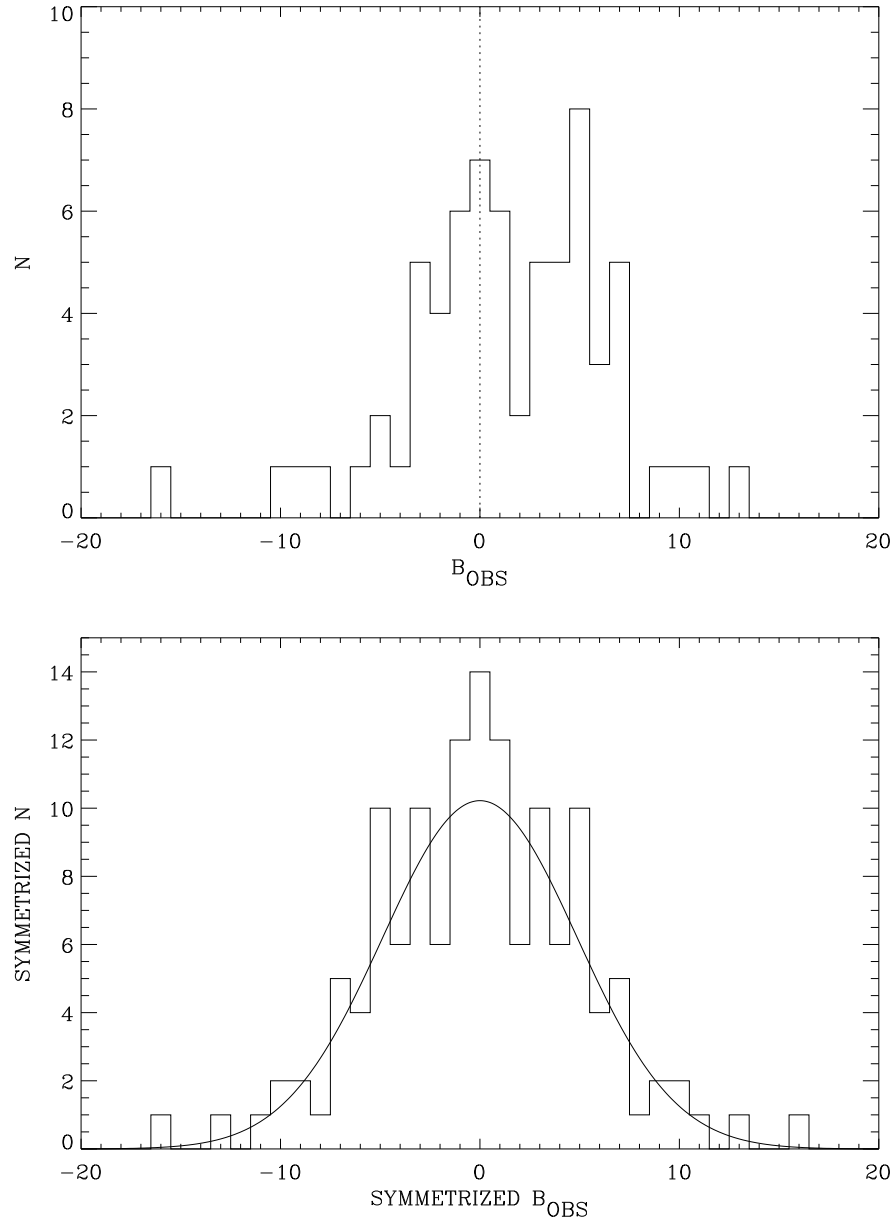


Fig. 4.— Top panel: the histogram of observed field strengths B_{obs} (in μG). Bottom panel: the same data, but symmetrized with each observation represented a second time with the opposite sign. The smooth curve is the Gaussian fit of equations 23.

$$\psi(B_{obs}) = \frac{1}{\sqrt{2\pi B_{obs,0}^2}} e^{-(B_{obs}^2/2B_{obs,0}^2)}, \quad (23a)$$

with

$$B_{obs,0} = 5.2 \pm 1.3 \text{ } \mu\text{G} . \quad (23b)$$

To find this best fit and error for $B_{obs,0}$, we numerically sampled a range of trial $B_{obs,0}$ values, and for each trial value compared the calculated cumulative distribution with that of the data by performing the Kolmogorov-Smirnov test. This provides sets of the K-S statistic D and its associated probability $P_{KS}(B_{obs,0})$ that the assumed distribution matches the observed one (see Press et al 1997). We determined the best fit for $B_{obs,0}$ by choosing the one that maximizes P_{KS} , which is $P_{KS} = 1.0$ (meaning that a Gaussian is an excellent fit), and we defined its uncertainty as being where the P_{KS} falls to 32% of its peak value (thus mimicking the definition of the 1σ error for Gaussian statistics).

Of course, the $5.2 \pm 1.3 \text{ } \mu\text{G}$ of equation 23b represents the pdf of B_{obs} . This is not the same as the pdf of B_{los} because of observational noise, which is very significant. Therefore, the dispersion of B_{los} is considerably smaller. Of course, it is B_{los} , not B_{obs} , which is the quantity of interest, so we need to statistically account for the observational noise. This is not straightforward because the 69 measurement errors are all different. If they had all been identical, then we could have used Gaussian statistics and convolutions to derive the true dispersion $B_{los,0}$ from the measured $B_{obs,0}$. Because the errors are not identical, we instead use a Monte Carlo analysis and employ the actual measurement uncertainties instead of their rms.

4.1.1. Monte Carlo Method

Here we use the observed values of B_{obs} , together with the uncertainties δB_{noise} , in a Monte Carlo simulation. We begin with four different possibilities for the functional form of $\phi(B_{tot})$; each of these is characterized by the median total field strength B_{tot} , and we calculate 46 uniformly spaced field possibilities ranging from 1 to $10 \text{ } \mu\text{G}$.

We assume random orientation with respect to the line of sight. We assume the observational errors δB_{noise} to be Gaussian-distributed. For each test possibility, we perform the set of 69 observations many times (20000 “trial runs”). Each time, for each of the 69 measurements we randomly generate a value of B_{tot} according to the assumed $\phi(B_{tot})$; orient it randomly with respect to the line of sight; derive its observed value B_{los} ; generate an uncertainty δB_{los} from a Gaussian pdf whose dispersion is equal to the associated value of δB_{noise} ; and record the resulting value of the observed $B_{obs} = B_{los} + \delta B_{los}$, which includes measurement errors. For each trial run,

all four possibilities for the functional form use the same values of B_{tot} , orientation, and δB_{los} . We make histograms of the absolute values B_{obs} and use the KS test to compare with the cumulative histogram of our data.

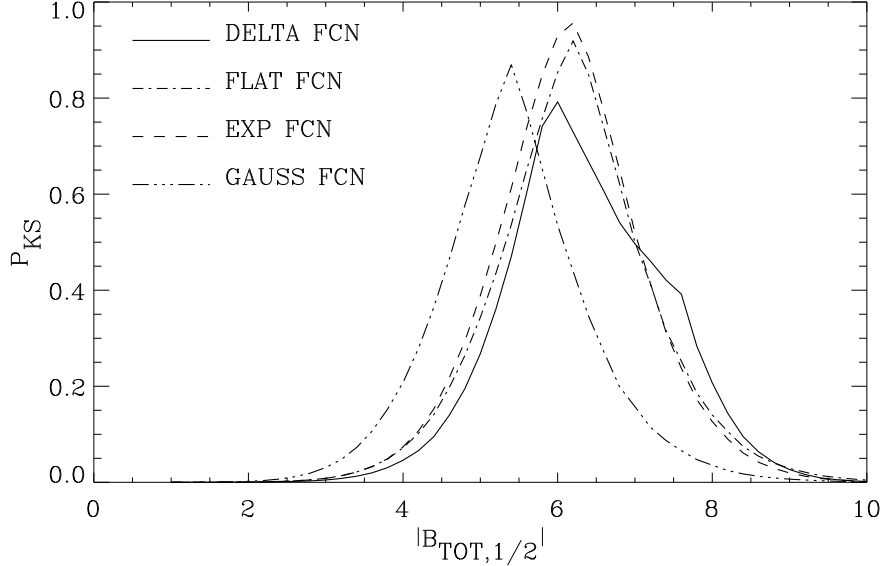


Fig. 5.— The KS fits of the Monte Carlo simulations for the four trial functional forms to the data, with the median $|B_{tot,1/2}|$ (in μG) as the independent variable.

Figure 5 displays the KS fits to the four functional forms. As anticipated in §3.1.1, all four KS fits are reasonably good, showing that the data cannot distinguish among these functional forms. However, medians for all four functional forms are quite similar, so the data do select the median with a reasonably small uncertainty.

To collapse the results of four functional fits into a single number for the median total field, we simply average the fields for the four peaks to obtain $6.0 \mu\text{G}$. To obtain the uncertainty, we use the maximum spread of the 32% points, which are 4.2 and $7.8 \mu\text{G}$. These combine to make our derived total median field strength

$$|B_{tot,1/2}| = 6.0 \pm 1.8 \mu\text{G} . \quad (24)$$

4.1.2. A Single Uncertainty δB_{noise} for Purposes of Convolution

Just above, in §4.1.1, we derived the median value $B_{tot,1/2} = 6.0 \mu\text{G}$. Under the assumption that the distribution of observed values *without* noise is Gaussian, then the pdf of B_{tot} is the

weighted exponential of equation 8. In this equation, the median $B_{tot,1/2} = 6.0 \mu\text{G}$ corresponds to $B_0 = 3.9 \mu\text{G}$.

This value of $B_0 = 3.9 \mu\text{G}$ is really $B_{los,0}$, i.e. it refers to what we would see *without* noise; in contrast, *with* noise we found $B_{0,obs} = 5.2 \mu\text{G}$. Thus, for this particular pdf for B_{tot} , our ensemble of B_{obs} is equivalent to convolving the ensemble of actual values B_{los} with a *single* Gaussian of dispersion

$$\delta B_{noise,sngl} = (5.2^2 - 3.9^2)^{1/2} = 3.4 \mu\text{G} . \quad (25)$$

Below, in our interpretation of bivariate histograms of our results, we will convolve the Monte-Carlo-derived values of B_{los} (which have no noise) with a Gaussian of this dispersion to obtain simulations of the measured histograms involving B_{obs} (which includes noise). This is a quick, approximate way to illustrate how measurement errors affect the histograms of observed values.

4.2. Derivation of the intrinsic $\phi(N_\perp)$ from the histogram of observed N_{los}

We first distinguish between two distinct sets of data for N_{los} and V_{los} . One is the entire sample of CNM components from Paper II. The second is the sample we have been discussing, namely that comprising the 69 statistically interesting measurements of B_{obs} ; these are drawn from Paper III, restricted to those having small uncertainties δB_{noise} . This smaller sample has a bias eliminating small column densities, which are irrevocably associated with large uncertainties in δB_{noise} .

We should not use the smaller dataset of 69 samples for discussing the statistics of column density and velocity, because it is biased. Instead, we use the larger dataset, but with some restrictions. We include all components from Paper II that satisfy the restrictions that $|b| > 10^\circ$, $V_{turb,los}^2 > 0$, and $V_{turb,los} < 5.25 \text{ km s}^{-1}$. The first restriction helps to eliminate blending of CNM components; the second eliminates 5 components for which the errors happen to yield $T_{kmax} < T_k$; and the third eliminates 3 outliers to the analytic approximation below. All this leaves us with 138 for the sample from Paper II. In the ensuing discussion, we will specify which dataset we are using.

4.2.1. A Preliminary: latitude dependence of N_\perp

In §4.2.2 below we will assume that the sheets are oriented randomly and derive the intrinsic $\phi(N_\perp)$ from the histogram of observed N_{los} . Before doing this, however, we consider whether the distribution is, in fact, random. In particular, we might expect the sheets to lie parallel to the Galactic plane, in which case we would expect $N_{los} \propto \frac{1}{\sin|b|}$, so we discuss this possibility first.

Figure 6 exhibits the latitude dependence of N_{los} . Looking at the points, one sees some higher values near smaller $|b|$, leading one to suspect that this might be a statistical trend. To test this

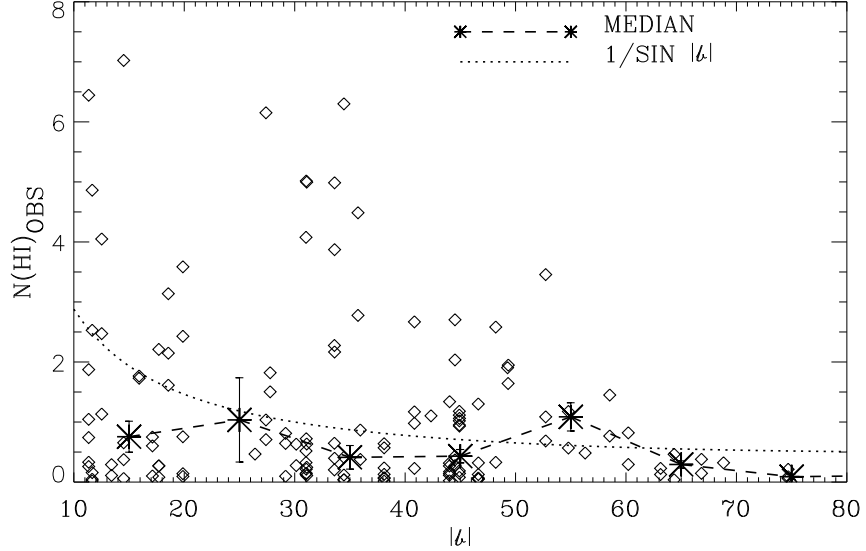


Fig. 6.— Diamonds are datapoints, N_{los} (in 10^{20} cm^{-2}) versus $|b|$. Each star represents the median of N_{los} within the 10° wide bin centered on the star; the stars are connected by the dashed line. The dotted line is $N_{los} = \frac{1}{\sin|b|}$, and is meant only to guide the eye. Two points, located at $(|b|, N(HI)) = (28, 12)$ and $(19, 13)$, are excluded from the figure (but not the medians) to save space.

suspicion we examine the latitude dependence of binned medians. The errorbars on the starred medians were calculated using the absolute values of the residuals, i.e. the error is $\frac{\sum|N_{los} - N_{los1/2}|}{M^{1/2}(M-1)}$, where $N_{los1/2}$ is the median and M is the number of points in the bin. The dashed line connects the medians of N_{los} for 10° -wide bins in $|b|$.

If $N_{los} \propto \frac{1}{\sin|b|}$, then these medians should follow the same dependence; we provide the dotted line, which is $N_{los} = \frac{1}{\sin|b|}$, for a visual comparison. Visually, there is absolutely no tendency for the medians to follow $\frac{1}{\sin|b|}$. The presence of datapoints with high N_{los} at small $|b|$ might be real or it might be a statistical artifact. If it is real, it might mean that sheets are in fact aligned with the Galactic plane to some degree and/or have their own intrinsic distribution of N_\perp .

There is more to this relationship than random statistics, namely our nonuniform and nonrandom sampling of the sky. Of course, we are restricted to Arecibo's sky, which is a 38° -wide swath in declination. In the vicinity of right ascension 04^h30^m it passes through the Taurus/Perseus region at $\ell \sim 180^\circ$, covering a large spread in latitude and a small range in longitude. Large column densities persist here up to $|b| \sim 50^\circ$, which is an anomaly in the overall latitude distribution of the neutral ISM. Thus in Taurus/Perseus, if we were to plot the *total* observed column density towards any direction (as opposed to N_{los} , which is the observed column density in one CNM Gaussian

component) versus $|b|$, it would not behave anything like $\frac{1}{\sin|b|}$. On the contrary, in other longitude ranges the situation differs. For example, in the vicinity of $\ell = 240^\circ$ the ISM column density is anomalously small. Thus, plotting quantities versus $|b|$ also plots them versus a biased distribution in ℓ . Accordingly, given the nonuniform sampling of the sky, it is very difficult to establish a latitude dependence.

From the above, we conclude that we cannot extract a latitude dependence of N_{los} from the data. Accordingly, we proceed under the simplest assumption, namely that the sheets are randomly oriented with respect to the observer's line of sight.

4.2.2. Derivation of $\phi(N_\perp)$ assuming the sheets are randomly oriented

The top panel of Figure 7 exhibits the histograms of observed column densities N_{los} together with a curve that, over most of the region, goes roughly as N_{los}^{-1} (see equation 27 below). The solid histogram is for the full Paper II sample of 138 datapoints. The eyeball tells us that this is a reasonably good fit. Using equation 11, we find that if $\psi(N_{los}) \propto N_{los}^{-1}$, then $\phi(N_\perp)$ has the same dependence, namely $\phi(N_\perp) \propto N_\perp^{-1}$. Unfortunately, its integral diverges so it is not a valid pdf. Rather, we must impose lower and upper limits on this pdf.

To proceed, we assume

$$\phi[N_\perp] = \begin{cases} \frac{\kappa}{N_\perp} & \text{if } N_{\perp min} \leq N_\perp \leq N_{\perp max} \\ 0 & \text{otherwise} \end{cases} \quad (26)$$

where $\kappa = [\ln(N_{\perp max}/N_{\perp min})]^{-1}$ and derive the corresponding $\psi(N_{los})$ from equation 11. This yields

$$\psi(N_{los}) = \begin{cases} 0 & N_{los} < N_{\perp min} \\ \kappa \frac{N_{los} - N_{\perp min}}{N_{los}^2} & N_{\perp min} \leq N_{los} \leq N_{\perp max} \\ \kappa \frac{N_{\perp max} - N_{\perp min}}{N_{los}^2} & N_{los} > N_{\perp max} \end{cases} \quad (27)$$

We then numerically cover a grid of trial values for $(N_{\perp min}, N_{\perp max})$ and for each combination derive the corresponding $\psi(N_{los})$. From that, we calculate the cumulative distribution and compare with the observed one by performing the K-S test, from which we obtain the bivariate probability $P_{KS}(N_{\perp min}, N_{\perp max})$ that the assumed distribution matches the observed one. We determine the best fit parameters by choosing the combination $(N_{\perp min}, N_{\perp max})$ that maximizes P_{KS} .

Figure 8 shows contour plots of $P_{KS}(N_{\perp min}, N_{\perp max})$. The top panel is for the 138 datapoints from Paper II, which is the larger and unbiased sample. The highest contour encloses a well-defined

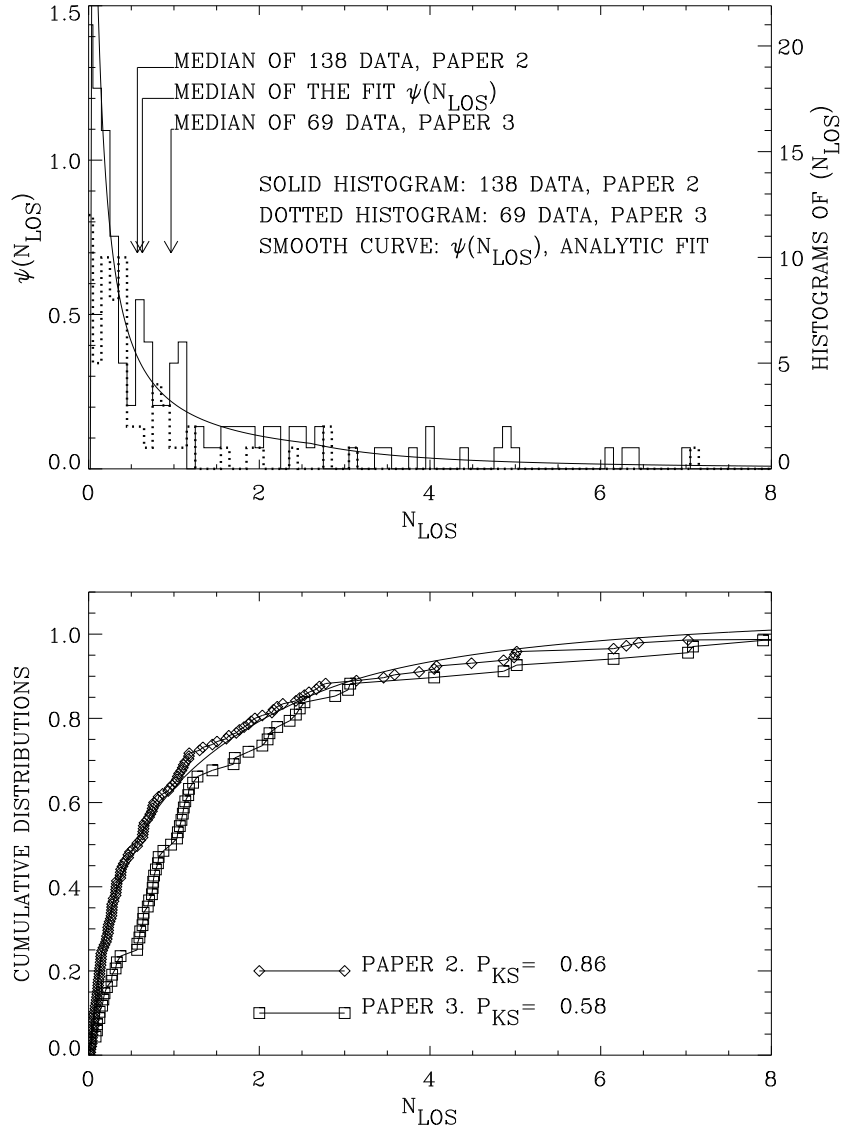


Fig. 7.— Analytic fit and observed distributions for N_{los} (in 10^{20} cm^{-2}). The solid histogram in the top panel is for the full set of 138 sheets from Paper II; the dashed is for the restricted set of 69 from Paper III, used in the present paper. The smooth curve is $\psi(N_{\text{los}})$, the pdf of equation 27, which is the analytic fit to the 138 datapoints; this curve closely follows N_{los}^{-1} . The bottom panel shows the three equivalent cumulative distributions; the diamonds are the solid histogram and the squares the dotted one.

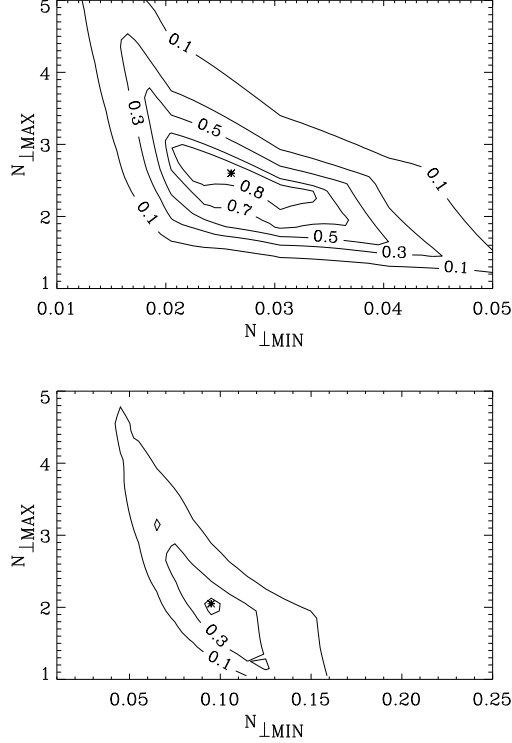


Fig. 8.— Contours of $P_{KS}(N_{\perp min}, N_{\perp max})$ (units are 10^{20} cm^{-2}). The stars are the adopted solutions for $(N_{\perp min}, N_{\perp max})$. Top panel, the 138 datapoints from Paper II; bottom panel, the 69 datapoints from paper III.

area that has two peaks with $P_{KS} \sim 0.89$ connected by a saddle. We don't regard the differences within the highest contour to be significant and we adopt the point indicated by a star as the best solution; here $P_{KS} = 0.86$. We adopt its uncertainty as defined by the contours where P_{KS} drops to ~ 0.30 , which is $\sim 32\%$ of the peak value 0.89. This yields

$$N_{\perp min} = 0.026_{-0.010}^{+0.019} \times 10^{20} \text{ cm}^{-2} \quad (28a)$$

$$N_{\perp max} = 2.6_{-1.2}^{+1.9} \times 10^{20} \text{ cm}^{-2} \quad (28b)$$

These two limits differ by two orders of magnitude! For most of the range of N_{\perp} between these limits, $\phi(N_{\perp}) \propto N_{\perp}^{-1}$ to a very good approximation. In Figure 7, the smooth solid line in the top panel is equation 27 with these values of $(N_{\perp min}, N_{\perp max})$. The bottom panel shows the cumulative distributions, both for the data (in diamonds) and for this derived pdf. To the eye the match looks excellent, and this is confirmed by the high value of the K-S probability $P_{KS} = 0.86$.

Figure 7 also shows the distributions for the current magnetically-selected sample 69 datapoints from Paper III. The top panel shows the histogram in a dotted line. The dotted histogram differs significantly from the solid one because it doesn't have the large increase for small N_{los} . The magnetic selection excludes datapoints whose uncertainty δB_{los} exceeds an upper limit. This restriction biases the column densities, because it is impossible to obtain small uncertainties on B_{los} for small N_{los} . Consequently, the pdf of N_{los} is cut off at small values. The bottom panel of Figure 8 shows contour plots of $P_{KS}(N_{\perp min}, N_{\perp max})$ for this set of 69 datapoints. Clearly, the contours peak at a different location. The bias in the magnetically selected points is reflected in the larger value of $N_{\perp min}$, 0.090 for the magnetically-selected sample versus 0.026 for the unbiased sample. The values of $N_{\perp max}$ are comparable: 2.0 and 2.6 for the small and large samples, respectively. The maximum value of $P_{KS} = 0.58$, indicating good agreement between the data and the analytic representation.

4.3. Derivation of the intrinsic $\phi(V_{turb})$ from the histogram of observed $V_{turb,los}$

The top panel of Figure 9 exhibits the cumulative distribution of the 138 $V_{turb,los}$ from Paper II (solid line), together with an adopted cumulative distribution (dashed line). We obtained the fit by trial and error: for trial functional forms for $\phi(V_{turb})$, we used equation 15 to calculate the corresponding $\psi(V_{turb,los})$. Trial functional forms included $\phi(V_{turb}) \propto x^n e^{-x}$, with $n = (0.25, 0.5, 1, 2)$, where $x = \frac{V_{turb}}{V_{turb,0}}$. The value $n = 1$ is significantly better than the others, resulting in $P_{KS} = 0.91$ for $V_{turb,0} = 1.06 \text{ km s}^{-1}$. This functional form is not unique: the function $\phi(V_{turb}) \propto x^{1/2} e^{-x^2}$ fits almost as well, with $P_{KS} = 0.81$ for $V_{turb,0} = 1.7 \text{ km s}^{-1}$. These line widths are dispersions. The middle panel shows the data histogram and corresponding pdf $\psi(V_{turb,los})$, and the arrow indicates the median of the observed distribution at $V_{turb,los,1/2} = 1.2 \text{ km s}^{-1}$. The bottom panel shows $\phi(V_{turb})$.

The above paragraph assumes the model in which V_{turb} is perpendicular to B_{tot} . If we drop that assumption, then the line-of-sight distribution of $V_{turb,los}$ has the same functional form as that of V_{turb} (but is narrower by $3^{1/2}$). A good fit for the observed distribution is $\psi(V_{turb,los}) \propto x^2 e^{-x}$, i.e. $n = 2$ in the above paragraph, with $V_{turb,los,0} = 0.45 \text{ km s}^{-1}$. This line width is dispersion.

5. DERIVATION OF PREDICTED BIVARIATE OBSERVED DISTRIBUTIONS AND COMPARISON WITH DATA

In this section, we use the previous determinations of the pdf of intrinsic quantities $\phi(B_{tot})$, $\phi(N_{\perp})$, and $\phi(V_{turb})$ to determine the expected bivariate distributions of observed pairs $\psi(B_{obs}, N_{los})$, $\psi(V_{turb,los}, B_{obs})$, and $\psi(V_{turb,los}, N_{los})$. If the observations were good enough, this would enable us to use the correlations among observed quantities to infer astrophysical model parameters. Unfortunately, we will find that we cannot.

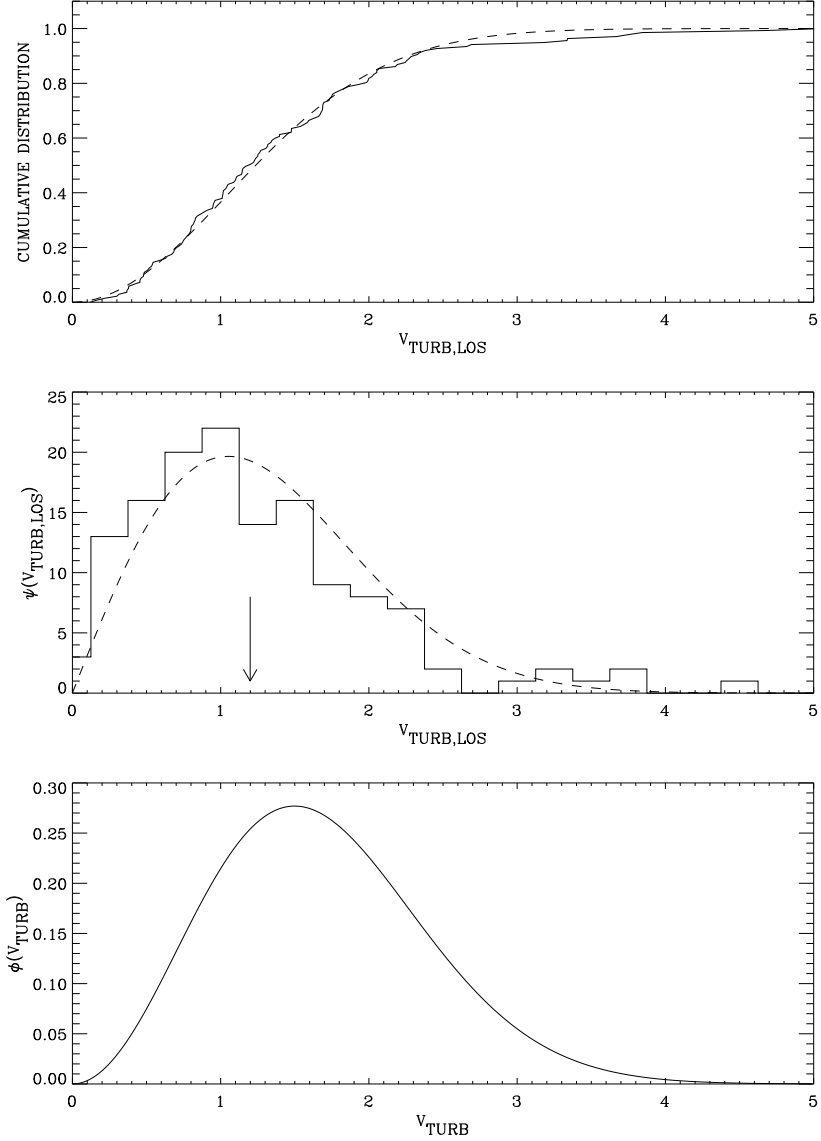


Fig. 9.— The top panel shows the fitted and actual cumulative distributions of $V_{turb,los}$ (in km s^{-1}). The middle panel shows the corresponding pdfs, i.e. the data histogram and $\psi(V_{turb,los})$. The third panel shows our fitted $\phi(V_{turb})$. The arrow shows the median of the observed histograms. Line widths are dispersions.

5.1. $\phi(B_{tot}, N_{\perp})$ and $\psi(B_{obs}, N_{los})$

Here we employ the observationally-derived univariate distributions for B_{tot} and N_{\perp} to predict the bivariate distribution of the observed quantities $\psi(B_{los}, N_{los})$, for the two cases of B_{tot}

perpendicular and parallel to the sheets. However, this single step does not provide a firm basis for comparison with the data because the observational uncertainties on B_{los} are so large.

As we saw in §4.1.1, the noise precludes our deriving even the univariate $\phi(B_{tot})$, so for discussion purposes we adopt the EXP FCN of equation 8 with $B_0 = 3.9 \mu\text{G}$ (which provides the required median value $6.0 \mu\text{G}$) (§4.1.1). Even with this, however, there is additional step: we must predict the bivariate distribution of the *measured* B_{obs} (which includes observational error), i.e. we must obtain $\psi(B_{obs}, N_{los})$ instead of $\psi(B_{los}, N_{los})$. We accomplish this by convolving the conditional distribution $\psi(B_{los} | N_{los})$ with a Gaussian having the rms measurement dispersion $3.4 \mu\text{G}$ (§4.1.2), and doing this as a function of N_{los} .

5.1.1. Case of \mathbf{B}_{tot} Perpendicular to the Sheet

Here we use equation 17 to predict the observed $\psi(B_{los}, N_{los})$ for the perpendicular case. As explained above, for $\phi(B_{tot})$ we use the EXP FCN of equation 8 with $B_0 = 3.9 \mu\text{G}$; and ϕ_{N_\perp} comes from §4.2. The analytic solution is somewhat cumbersome and yields

$$\psi(B_{los}, N_{los}) = \begin{cases} \frac{\kappa\sqrt{2}}{\sqrt{\pi}B_0N_{los}} \left[e^{-[B_{los}^2/(2B_0^2)]} - e^{-[B_{los}^2N_{los}^2/(2B_0^2N_{\perp min}^2)]} \right] & N_{los} \leq N_{\perp max} \\ \frac{\kappa\sqrt{2}}{\sqrt{\pi}B_0N_{los}} \left[e^{-[B_{los}^2N_{los}^2/(2B_0^2N_{\perp max}^2)]} - e^{-[B_{los}^2N_{los}^2/(2B_0^2N_{\perp min}^2)]} \right] & N_{los} > N_{\perp max} \end{cases} \quad (29)$$

This produces contours in the (B_{los}, N_{los}) plane; Figure 10, top panel, shows the results. The version including measurement errors is in the middle panel.

The general trend in the top panel is clear from the discussion of §2: large measured column densities N_{los} produce small measured fields B_{los} because the field lines are perpendicular to the sheets. Unfortunately, including the observational uncertainties, as we do in the middle panel, obscures this trend. We defer further discussion to §6.

5.1.2. Case of \mathbf{B}_{tot} Parallel to the Sheet

Here we proceed as in §5.1.1, but use equation 19 instead of equation 17 to predict the observed $\psi(B_{los}, N_{los})$ for the parallel case. The math is complicated, so we proceed by calculating $\psi(B_{los}, N_{los})$ using a Monte Carlo simulation. Figure 11 shows the results. The version including measurement errors is in the middle panel.

The general trend in the top panel is clear from the discussion of §2: for $N_{los} \gg N_{\perp max}$, we see sheets more nearly edge-on where B_{los} is usually large and the conditional pdf $\psi(B_{los} | N_{los})$ becomes independent of N_{los} . We defer further discussion to §6.

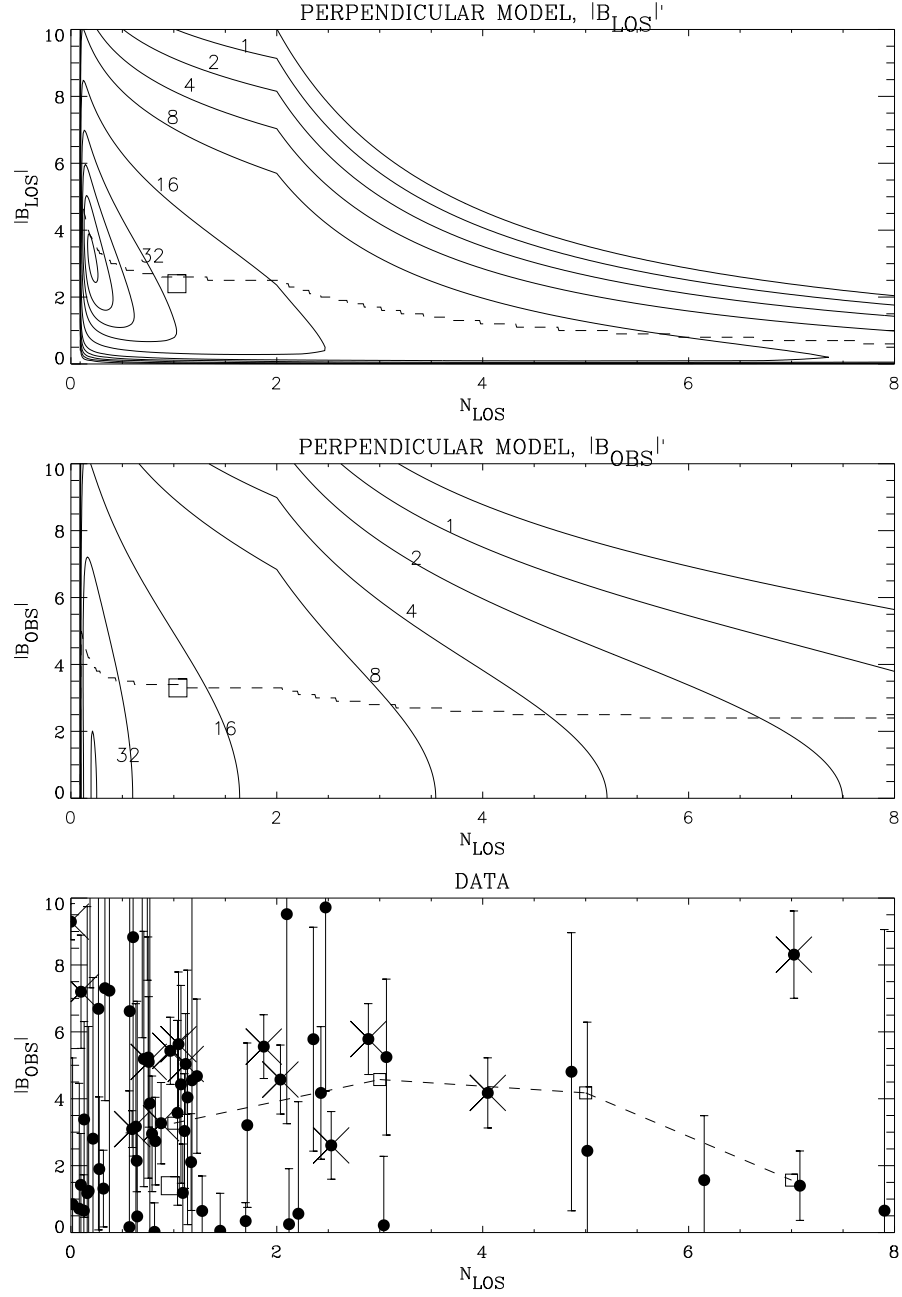


Fig. 10.— Top panel, contours from equation 29 of $\psi(B_{\text{LoS}}, N_{\text{LoS}})$ for the perpendicular case derived using the observationally-derived $\phi(B_{\text{tot}}, N_{\perp})$. Units are μG and 10^{20} cm^{-2} . The middle panel shows $\psi(B_{\text{obs}}, N_{\text{LoS}})$, which includes measurement errors on B_{LoS} . The square marks the univariate medians. Bottom panel, the data.

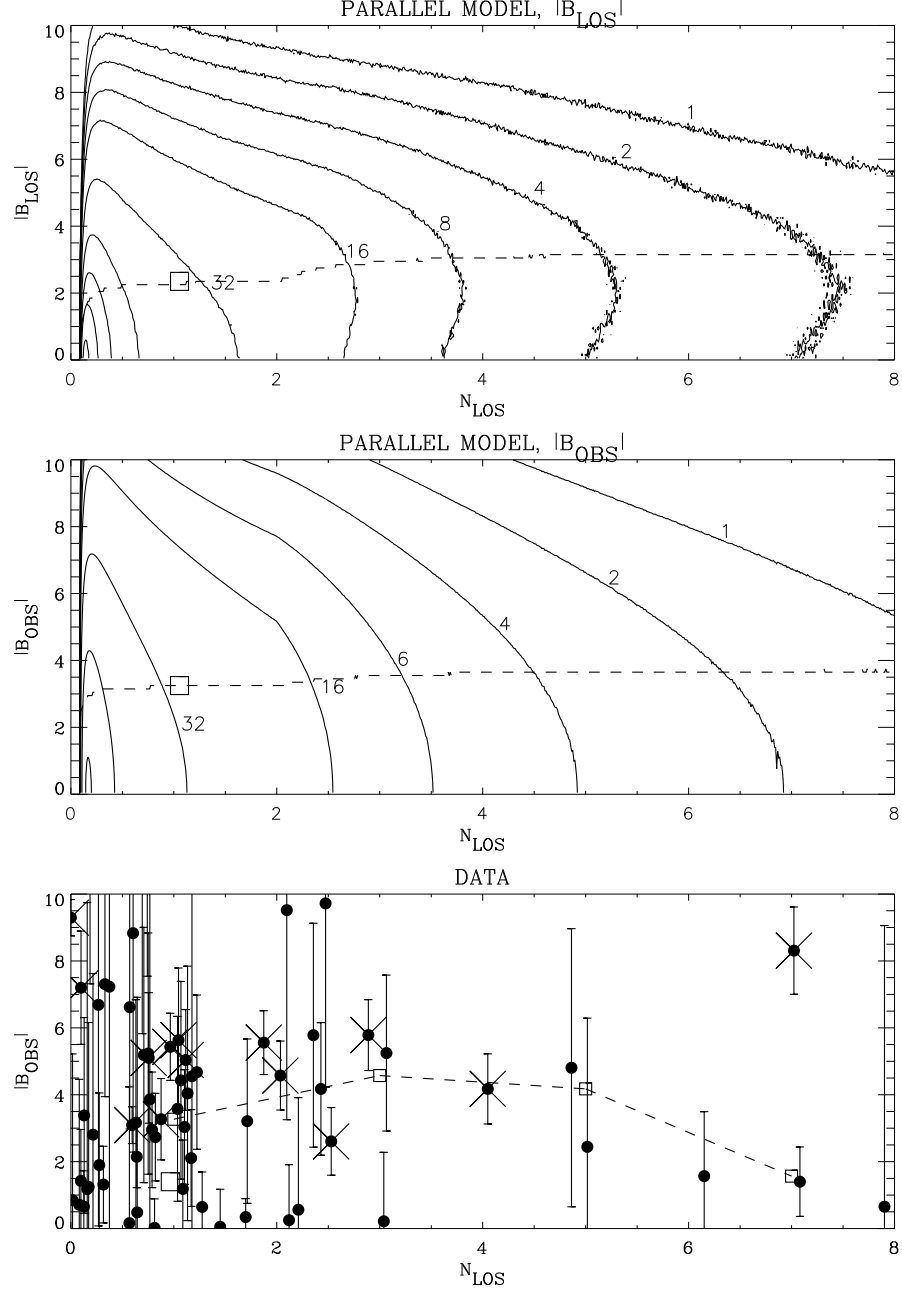


Fig. 11.— Top panel, contours of $\psi(B_{\text{los}}, N_{\text{los}})$ from a Monte Carlo simulation for the parallel case derived using the observationally-derived $\phi(B_{\text{tot}}, N_{\perp})$. Units are μG and 10^{20} cm^{-2} . The middle panel shows $\psi(B_{\text{obs}}, N_{\text{los}})$, which includes measurement errors on B_{los} . The square marks the univariate medians. Bottom panel, the 69 datapoints from Paper III.

5.2. $\phi(V_{turb}, B_{tot})$ and $\psi(V_{turb,los}, B_{los})$

As noted in §3.3.1, the bivariate distribution does not depend upon any model regarding the geometrical shape of the HI clouds. Figure 12, top panel, shows contours of $\psi(V_{turb,los}, B_{los})$ from a Monte Carlo simulation using the observationally-derived $\phi(V_{turb}, B_{tot})$; these B_{los} do not include measurement errors. The middle panel shows $\psi(V_{turb,los}, B_{obs})$ and the bottom panel shows the data. Contours are spaced by a factor of two. The eyeball says that the fit to these 69 datapoints is not bad, which makes it tempting to conclude that the turbulence is, in fact, perpendicular to the magnetic field. Unfortunately, however, the eyeball also says that the distribution of points doesn't differ much from one in which $|B_{obs}|$ and $V_{turb,los}$ are uncorrelated, meaning that such a conclusion is unwarranted.

5.3. $\phi(V_{turb}, N_{\perp})$ and $\psi(V_{turb,los}, N_{los})$

Here, as above with the relationship between B_{los} and N_{los} , the predicted bivariate distribution depends on whether the magnetic field is perpendicular or parallel to the sheet. Figure 13, top panel, shows contours of $\psi(V_{turb,los}, B_{los})$ for the perpendicular model; the middle panel shows the parallel model. The contours are derived from Monte Carlo simulations using the observationally-derived $\phi(V_{turb}, N_{\perp})$, assuming that two quantities are independent. The bottom panel shows the data.

Unfortunately, the difference between the contours in the top and middle panel is not large and it doesn't take a quantitative analysis to tell that the data cannot distinguish between the two models. To the eye, the data look in reasonable agreement with both models.

6. WHICH SHEET MODEL FITS BETTER?

The key to distinguishing between the two sheet models is the bivariate distributions because the univariate distributions don't depend on whether the perpendicular or parallel model reigns. Of the three bivariate distributions, two are relevant.

Figure 13 displays $\psi(V_{turb,los}, N_{los})$. Unfortunately, the differences between the contours in the top panel (perpendicular model) and middle panel (parallel model) are not large. We can make a quantitative comparison of these bivariate distributions with the data by using the two-dimensional generalization of the K-S test described by Press et al (1997), which provides P_{KS} in a similar fashion as does the usual one-dimensional K-S test. The values are $P_{KS} = 0.032$ and 0.016 for the perpendicular and parallel cases, respectively. These values are both small, but not so so small as to rule out agreement of the data with the model. They differ by a factor of two, but this is nowhere near enough of a difference to distinguish between the two cases. Moreover, our basic assumption in deriving these distributions is the anisotropy of the turbulent velocity V_{turb} , which

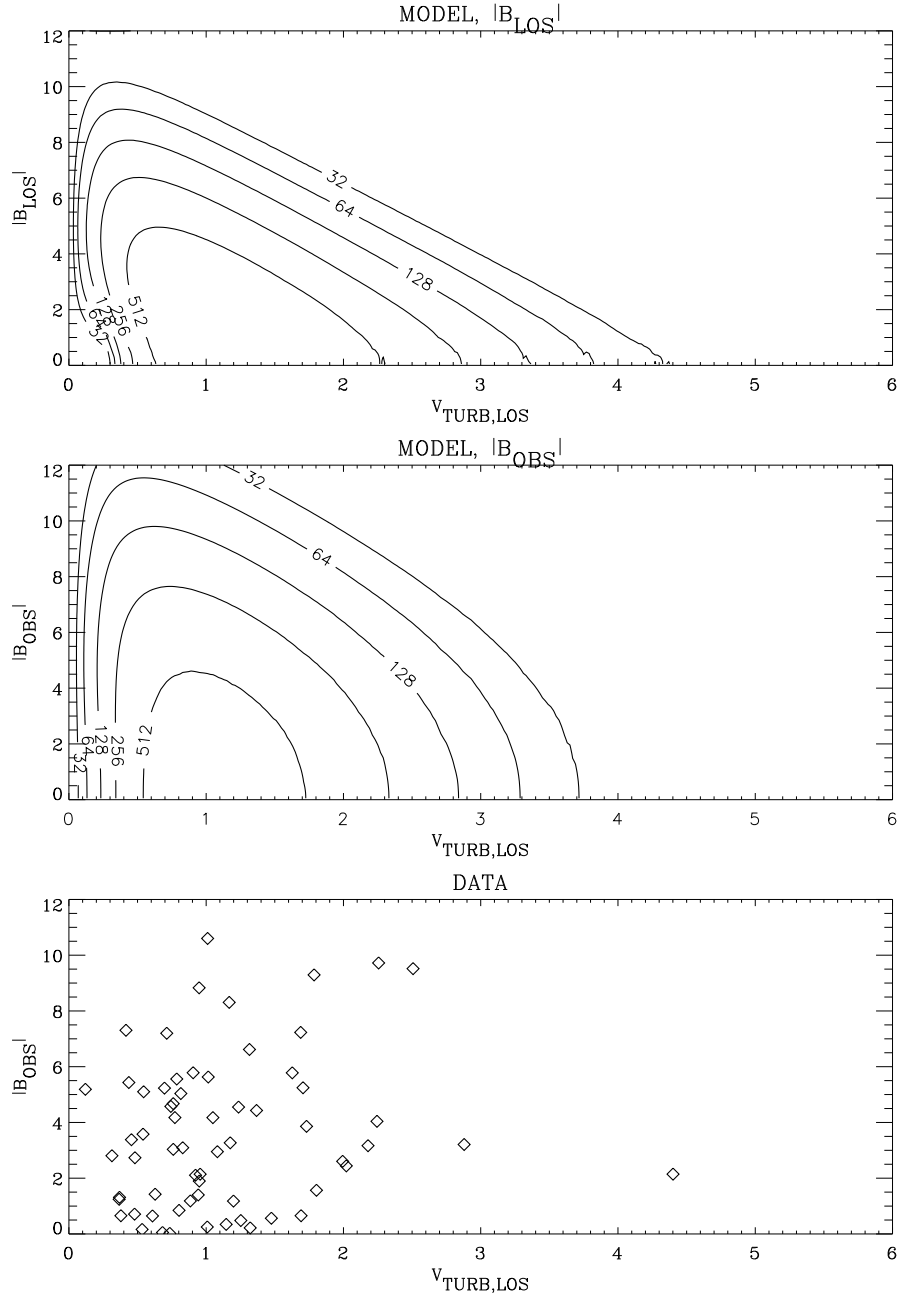


Fig. 12.— Top panel, contours of $\psi(V_{\text{turb,los}}, B_{\text{los}})$ from a Monte Carlo simulation using the observationally-derived $\phi(V_{\text{turb}}, B_{\text{tot}})$. Units are km s^{-1} and μG . The middle panel shows $\psi(V_{\text{turb,los}}, B_{\text{obs}})$, which includes measurement errors on B_{los} . Bottom panel, the data.

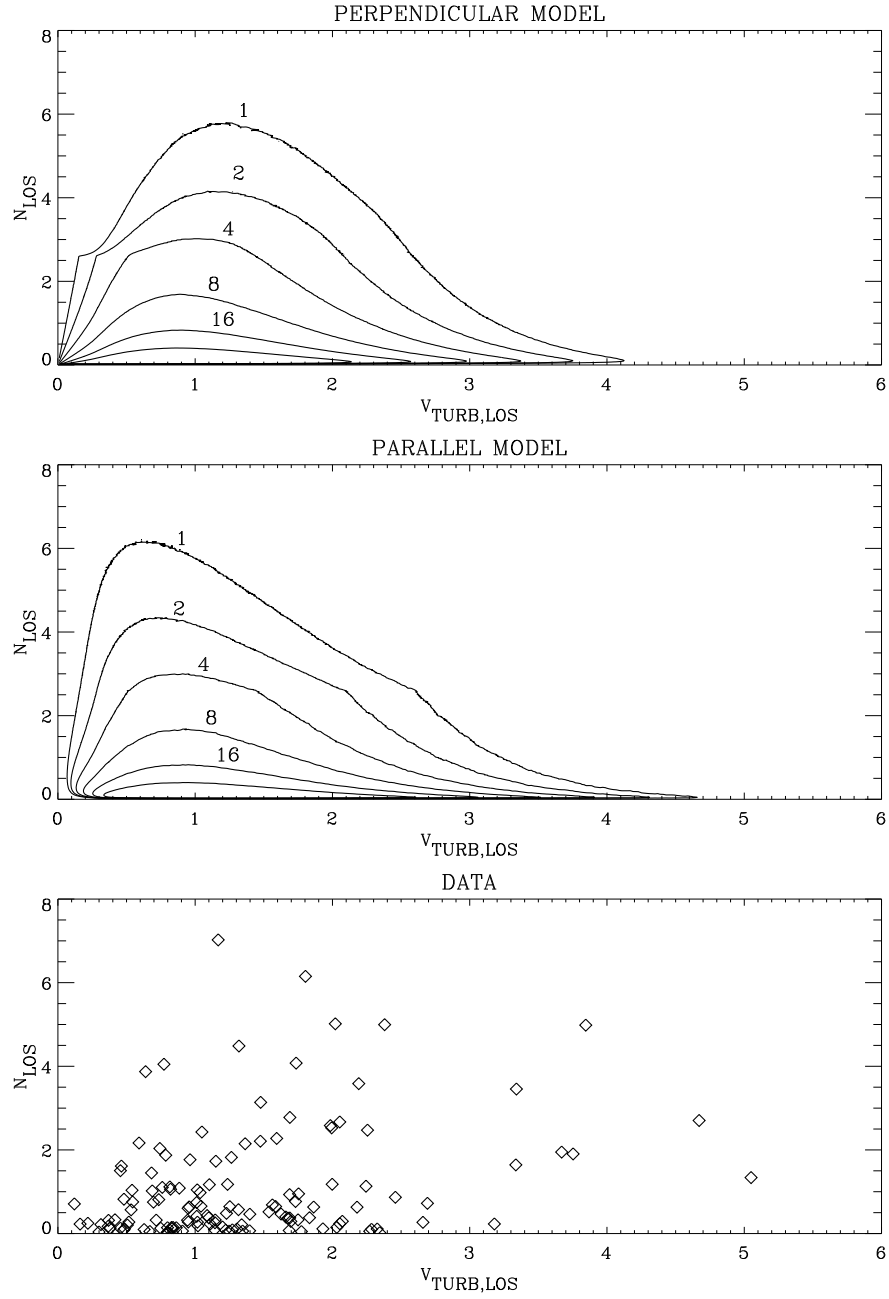


Fig. 13.— Contours of $\psi(V_{\text{turb},\text{los}}, N_{\text{los}})$ from a Monte Carlo simulation using the observationally-derived $\phi(V_{\text{turb}})$ and $\phi(B_{\text{tot}})$. Units are km s^{-1} and 10^{20} cm^{-2} . Top and middle panels show the perpendicular and parallel sheet models, respectively. Bottom panel shows the data.

might not be correct. Unfortunately, this bivariate distribution cannot distinguish between the two models.

The bivariate pair $\psi(N_{los}, B_{los})$ is more directly related to the two models because there is no additional assumption involving anisotropy of the turbulence. Figures 10 and 11 exhibit the pair for the perpendicular and parallel cases, respectively. After including the measurement errors (middle panels), the two bivariate distributions look similar, as do the runs of the median $B_{obs,1/2}$ versus N_{los} . Neither represents the data very well. We can be quantitative and perform the two-dimensional K-S test, as above; the perpendicular and parallel cases yield $P_{KS} = 0.022$ and 0.024 , respectively. Again, the values are small but not so small as to rule out the models; and, again, the test cannot distinguish between the two cases.

One can argue that the single reliably-detected point at $(N_{los}, B_{los}) \sim (7, 8 \mu\text{G})$ is more consistent with the parallel model, for which the two quantities tend to be correlated. This particular Gaussian component of 3C142.1 (Paper III) has among the largest values for both quantities, which means that for the perpendicular model we need either a *very* thick sheet and/or a *very* high intrinsic field strength. But we cannot extend this argument to other sources, whose values are more representative.

A confident choice of model requires more and better data. Unfortunately, this is not likely given current instrumentation, because we have already used ~ 800 hours of Arecibo time for this project.

7. ASTROPHYSICAL DISCUSSION: MAGNETIC FIELDS

7.1. Observational issues

As discussed in §3.1.1, we observe the line-of-sight component of magnetic field B_{los} , which is always less than the actual magnetic field B_{tot} . Figure 1 and its associated discussion shows that, in practice, we cannot determine the intrinsic distribution $\phi(B_{tot})$ from observations of B_{los} . Fortunately, the median is well-determined, with $|B_{tot,1/2}| = 6.0 \pm 1.8$ (§4.1.1).

Figure 1 and Table 1 show that the median line-of-sight field strength $B_{los,1/2}$ is less than half that of the total field $B_{tot,1/2}$, with most of the histograms of $\psi(|B_{los}|)$ peaking at zero. This functional behavior of B_{los} , which results purely from geometry, is responsible for the large number of nondetections in our sample. Moreover, it explains particular cases where B_{los} is small. A spectacular example is the local-arm field seen against Cas A, $B_{los} = -0.3 \pm 0.6 \mu\text{G}$. This surprisingly small result is perfectly consistent with statistical expectation. Of course, we cannot rule out that the field actually is really small in any particular case like this, but one needs additional data to draw such a conclusion!

Now consider the large set of magnetic fields observed in 21-cm line *emission* in morphologically

obvious structures, reviewed by Heiles & Crutcher (2005). The term “morphologically obvious” means filaments or edge-on sheets. Edge-on sheets should be edge-on shocks in which the field is parallel to the sheet. Here, the statistics reverse and favor relatively large B_{los} . As explained in §3.2.3, as the line of sight becomes parallel to the sheet—i.e., for a morphologically obvious sheet—the median $B_{tot1/2} \rightarrow 0.71B_{tot}$. For these structures, measured fields are strong, ranging from ~ 5 to $\sim 10 \mu\text{G}$. This is not inconsistent with a uniform $B_{tot} \sim 10 \mu\text{G}$, which is almost a factor of two above the median CNM field strength. This suggests that shocks enhance the field strength, but not by large factors.

Finally, compare the CNM median field $B_{tot1/2}$ with other estimates of field strength. Beck (2003) reviews the most recent estimate of field strength derived from synchrotron emission, minimum energy arguments, measured cosmic ray flux, and polarization. He finds the regular component to be $\sim 4 \mu\text{G}$ and the total component to be $\sim 6 \mu\text{G}$. Pulsars give a much smaller value for the regular component, but they provide an underestimate if field and electrons are uncorrelated, as is likely (Beck et al 2003); nevertheless, they give about $5 \mu\text{G}$ for the total component (review by Heiles 1996).

The difference between the regular and total components is the fluctuating component, whose turbulent spectrum covers a wide range of scales ranging up to at least tens of parsecs (e.g., the North Polar Spur). Our CNM structure sizes are typically of order tenths of a parsec (Paper III), smaller than much of the magnetic field’s turbulence scale range. For this reason we think that it is more appropriate to compare the CNM field strengths with the total component given by Beck, not the regular one. Our CNM median of $\sim 6.0 \mu\text{G}$ is close to the local Galactic total component of $\sim 6 \mu\text{G}$.

7.2. Astrophysical issues

We find that B_{tot} in the CNM is comparable to the field strength in other ISM components. This is at first surprising because the volume density $n(\text{HI})$ in the CNM greatly exceeds that in all other interstellar structures except molecular clouds. Flux freezing applies almost rigorously in the diffuse gas, even in the HI, and as the interstellar HI changes from CNM to WNM and back again, whether by thermal instability or dynamical processes, the transition must occur under the constraints imposed by flux freezing. Under the usual flux-freezing ideas, magnetic field strength should increase with volume density. If this increase would actually occur, then we would expect higher field strengths in the CNM than in other diffuse gas phases because the ISM should exhibit approximate thermal pressure equality among the phases. This evidently doesn’t happen. In fact, this absence of field strength increase for small $n(\text{HI})$ is well known from past studies (e.g. Crutcher, Heiles, & Troland 2003, section 3.4), so this is hardly news.

The field is strong enough to dominate the gas pressure, and therefore the dynamics. With a CNM median field $B_{tot} \sim 6.0 \mu\text{G}$, which also applies elsewhere in the interstellar volume, the

magnetic pressure is $\frac{P_{mag}}{k} \sim 10400 \text{ cm}^{-3}$ K. This dominates the CNM pressure $P_{CNM} \sim 3000 \text{ cm}^{-3}$ (Jenkins & Tripp, 2001; Wolfire et al, 2003). When the field dominates the pressure, it is much less affected by the gas pressure or thermodynamic state.

CNM structures are magnetically subcritical. When gravitation is important, the distinction between magnetically sub- and supercritical clouds occurs at $\frac{B_{tot}}{N_{\perp}} \sim 0.38$ (Nakano & Nakamura 1978). In subcritical clouds, the magnetic field dominates gravity and prevents collapse. Our CNM sheets have $N_{\perp} \lesssim 2.6$ and the median $B_{tot1/2} \sim 6.0 \mu\text{G}$, yielding a minimum ratio ~ 2.3 , far above the supercritical upper limit. Gravity is far from important in these clouds, but if several clouds were to coalesce into a gravitationally-important one then magnetic forces would prevent gravitational collapse—unless the field were destroyed in the process, e.g. by the annihilation of oppositely-directed fields during coalescence of individual clouds. In this sense, the field is strong and must dominate the act of star formation in denser clouds that form from less dense interstellar gas.

8. ASTROPHYSICAL DISCUSSION: COLUMN DENSITIES

It is well accepted that interstellar HI often lies in sheets. Paper II showed this convincingly for the CNM structures. In the present paper, we noted that the observed histogram of observed column density N_{los} falls monotonically with behavior close to N_{los}^{-1} . We then derived the pdf of the intrinsic column density for the sheets N_{\perp} and found that it follows equation 27 between two limits, which are rather well defined. Equation 27 behaves much like a N_{\perp}^{-1} distribution. Figure 7 convincingly shows that this is a good description of the observations.

Suppose, first, that the CNM results from shocks. We have in mind the McKee & Ostriker (1977) model, in which a supernova shock adiabatically compresses and heats the ambient gas; as the gas cools, it does so under roughly constant pressure so its density increases, it cools faster, and soon becomes the CNM. As the shocked gas cools it slows. For low-velocity CNM, which is primarily what we observe, the swept-up column density depends on the energy injected and the ambient density. This dependence is complicated (Cioffi, McKee, & Bertschinger 1988), so we don't attempt a detailed discussion. However, the swept-up column densities are not incomparable with our upper limit $N_{\perp max} = 2.6 \times 10^{20} \text{ cm}^{-2}$ in equations 27 and 28. Thus, the $\sim N_{\perp}^{-1}$ dependence in equation 27 could be a reflection of the statistical distribution of the relevant function of injected energy and ambient density.

Another possibility is that the CNM arises from kinematical and thermal processes in the turbulent interstellar medium. We have in mind structures like those seen in numerical simulations of interstellar turbulence such as Vázquez-Semadeni, Gazol, & Scalo (2000; see references in Paper II). Consider the “Triad region” discussed in extensively in §8.2 of Paper II and Heiles & Crutcher (2005). It has line-of-sight extent $\sim 0.05 \text{ pc}$ and plane-of-sky extent $\sim 20 \text{ pc}$, for an aspect ratio ~ 200 . It also has typical turbulent velocity $\sim 1 \text{ km s}^{-1}$, which makes the line-of-sight crossing

time $\sim 5 \times 10^4$ yr. This is very short—interstellar kinematical evolution over human history! If this sheet were the result of a slowed shock, it seems remarkable that, in the presence of ISM density fluctuations, the distance over which the swept-up column density is accumulated would allow the sheet to appear so coherent, and further that it would retain its coherence to be observable. The alternative is, we suppose, that CNM structures are transient, and that we can map as extensive only those that currently appear to be coherent.

This N_{\perp}^{-1} behavior does not seem to be a capricious result. Rather, it is a challenge to the theorists to reproduce it. Deciding between the above two possibilities, or others, is a matter of the explanation reproducing the N_{\perp}^{-1} behavior.

9. ASTROPHYSICAL DISCUSSION: TURBULENT VELOCITIES

In §4.3 we modeled the turbulent velocities as being anisotropic, i.e. perpendicular to the magnetic field, and derived the intrinsic pdf $\phi(V_{turb})$ from the observed one $\psi(V_{turb,los})$. Here V_{turb} is the the 1d component of turbulent velocity; for the 2d case we modeled, the full component is $2^{1/2}V_{turb}$. In §5.2 we discussed the bivariate distribution $\psi(V_{turb,los}, B_{obs})$. The data fit the model with anisotropic turbulence quite well, but the data also fit no correlation quite well, so the results are inconclusive. The observations cannot distinguish between anisotropic and isotropic turbulent velocities.

We can, however, discuss topics such as the relative energy densities in turbulent motions and magnetism, that is, whether turbulent velocities are superAlfvénic. Doing this requires some care in definitions of parameters: we measure line-of-sight turbulent velocity dispersions and these must be converted to their 2- or 3-dimensional counterparts; and we must include He as a component of the ISM mass density. Finally, we can discuss results in terms of the conventional plasma parameter β , in terms of energy densities, or in terms of supersonic and superAlfvénic.

First we define velocities and the Mach number. Let $\Delta V_{turb,1d}$ be the 1d turbulent velocity dispersion and $\Delta V_{th,1d}$ be the thermal velocity dispersion. For isotropic turbulence, the full turbulent velocity is $\Delta V_{turb} = \Delta V_{turb,3d} = 3^{1/2}\Delta V_{turb,1d}$. With this isotropic turbulence, the turbulent Mach number M_{turb} is

$$M_{turb}^2 = \frac{3\Delta V_{turb,1d}^2}{C_s^2} \quad (30)$$

Here C_s is the velocity of sound; the appropriate sound velocity is the isothermal one because thermal equilibrium is reached quickly in the CNM, so

$$C_s^2 = \frac{nkT}{\rho} \quad (31a)$$

The volume density is

$$\rho = (1 + 4f_{He})n_H m_H \quad (31b)$$

where f_{He} is the fractional abundance of He by number and m_H is the mass of the H atom; we adopt $f_{He} = 0.1$. Similarly, for the Alfvén velocity V_{ALF} , we have

$$V_{ALF}^2 = \frac{B_{tot}^2}{4\pi\rho} \quad (32)$$

The information propagation velocity perpendicular to the field lines is equal to the Alfvén velocity V_{ALF} . The mean square velocity perpendicular to the field lines is twice the line-of-sight value. Consequently, we define the Alfvénic turbulent Mach number $M_{ALF,turb}$ as

$$M_{ALF,turb}^2 = \frac{2\Delta V_{turb,1d}^2}{V_{ALF}^2} \quad (33)$$

If $M_{ALF,turb} > 1$, then shocks will develop; this is the superAlfvénic case.

Next we define energy densities. The turbulent energy density is

$$E_{turb} = \frac{\rho F \Delta V_{turb,1d}^2}{2} \quad (34)$$

Here we include the quantity F to allow for anisotropic turbulence. If turbulent velocities are only perpendicular to B , then $F = 2$; isotropic turbulence has $F = 3$ (the case assumed in paper II). Of course, the magnetic energy density is

$$E_{mag} = \frac{B_{tot}^2}{8\pi} \quad (35)$$

The ratio is

$$\frac{E_{turb}}{E_{mag}} = \frac{F \Delta V_{turb,1d}^2}{V_{ALF}^2} = \frac{F}{2} M_{ALF,turb}^2. \quad (36)$$

Finally, we define the conventional plasma parameter β_{th} , which compares thermal and magnetic pressures:

$$\beta_{th} \equiv \frac{P_{th}}{P_{mag}} = \frac{2\Delta V_{th,1d}^2}{V_{ALF}^2} \frac{1 + f_{He}}{1 + 4f_{He}} \quad (37)$$

For comparison of turbulent and magnetic effects, we calculate the relevant ratios for the following adopted parameter values, which are close to the medians:

$$T_{CNM} = 50 \text{ K} ; \quad (38a)$$

$$\frac{P_{CNM}}{k} = 3000 \text{ cm}^{-3} \text{ K} ; \quad (38b)$$

$$n(HI)_{CNM} = 54 \text{ cm}^{-3} ; \quad (38c)$$

$$\Delta V_{turb,1d} = 1.2 \text{ km s}^{-1} ; \quad (38d)$$

$$B_{tot} = 6.0 \text{ } \mu\text{G} . \quad (38e)$$

Here T is a typical CNM temperature from Paper II. P_{CNM} is from Jenkins & Tripp (2001) and Wolfire et al. (2003). The value for $\Delta V_{turb,1d} = 1.2 \text{ km s}^{-1}$ is the median from §4.3. The value for B_{tot} is the median from §4.1.1.

These values provide

$$M_{turb} = 3.7 ; \quad (39a)$$

$$\beta_{th} = 0.29 ; \quad (39b)$$

$$M_{ALF,turb}^2 = 1.3 ; \quad (39c)$$

$$V_{ALF} = 1.5 \text{ km s}^{-1} . \quad (39d)$$

If the field were small, then turbulence would be isotropic with $F = 3$. However, it is not so small, but neither is it so large that we could say for certain that $F = 2$. The limits $2 < F < 3$ correspond to $1.3 < \frac{E_{turb}}{E_{mag}} < 1.9$.

These values should be regarded as representative. Not all CNM clouds have the median values, so these parameters have a considerable spread.

One interesting question is whether *any* CNM Clouds have high β_{th} , i.e. whether any CNM clouds have negligible magnetic field. We cannot answer this because $\beta_{th} \propto \frac{P}{B_{tot}^2}$ and neither P nor B_{tot}^2 is attainable for an individual cloud. Moreover, the functional form of B_{tot} is ill determined: we cannot even distinguish between all values being the same (a delta-function distribution) and a Gaussian (which has a significant population of very high field strengths); see §4.1.1.

10. FINAL COMMENTS: TURBULENT AND MAGNETIC ENERGY EQUIPARTITION

Our numbers indicate that magnetism and turbulence are in approximate equipartition. The approximate equipartition suggests that turbulence and magnetism are intimately related by mutual exchange of energy. In the absence of turbulence, magnetic energies do not dissipate because the magnetic field cannot decay on short time scales. But with turbulence, the field may be able to decay rapidly (Heitsch & Zweibel 2003; Lazarian & Visniac 1999; Zweibel 2002). Moreover, numerical simulations suggest that supersonic turbulence also dissipates rapidly, even when the field is strong (MacLow et al 1998). However, it is not obvious to us that these dissipative processes should lead to the observed equipartition between turbulence and magnetism.

We suspect the answer lies in Hennebelle & Perault's (1999) result and Maclow's (private communication) observation that the CNM components result from the transient nature of turbulent flow: the CNM occupies regions where densities are high, produced by converging flows, and the density rise is limited by pressure forces. These limiting pressures are magnetic because the gas has small β_{th} , meaning that thermal pressure is negligible and the dynamical equality makes the magnetic pressure comparable to the converging ram pressure and leads to apparent equipartition.

The equipartition looks like a steady-state equilibrium, but it is really a snapshot of time varying density fields and our immediate observational view is a statistical result over a large sample. In other words, our current observational snapshot shows an ensemble at a given time. Against this we compare the numerical simulations, which are stationary in the sense that they have been allowed to run long enough that the statistical properties become time-independent. Such simulations are also ergodic, with statistical properties over time being equivalent to those over space. With this view, the ISM dynamically evolves through turbulence and its properties are governed by statistical equilibrium of energy inputs and dissipation. These matters are discussed at length in the excellent review by MacLow & Klessen (2004)

It is a pleasure to acknowledge discussions with Martin Bureau, Jeremy Darling, Avinash Deshpande, Doug Finkbeiner, Patrick Hennebelle, Dave Hollenbach, Mordecai MacLow, and Chris McKee. This work was supported in part by NSF grants AST-9530590, AST-0097417, AST-9988341, and AST 04-06987; and by the NAIC.

REFERENCES

Beck, R. 2003, in *How does the Galaxy work?*, ed. E.J. Alfaro, E. Perez & J. Franco, Kluwer.
Beck, R., Shukurov, A., Sokoloff, D., & Wielebinski, R., 2003, *A&A*, in press.
Cioffi, D.F., McKee, C.F., & Bertschinger, E. 1988, *ApJ*, 334, 252.

Crutcher, R.M., Heiles, C., & Troland, T.H. 2003, in *Turbulence and Magnetic Fields in Astrophysics*, ed. E. Falgarone & T. Passot, Springer, p. 155.

Heiles, C. 1996, in *Polarimetry of the Interstellar Medium*, eds W.G. Roberge & D.C.B. Whittet, ASP Conf Ser 97, San Francisco, p. 457.

Heiles, C. & Troland, T.H. 2003, *ApJ*, 586, 1067 (Paper II).

Heiles, C. & Troland, T.H. 2004, *ApJS*, 151, 271 (Paper III).

Heiles, C. & Crutcher, R.M. 2005, in *Magnetic Fields in the Universe*, ed. R. Wielebinski, Springer, in press.

Heitsch, F. & Zweibel, E. G. 2003, *ApJ*, 583, 229.

Hennebelle, P. & Perault, M. 1999, *A&A*, 351, 309.

Jenkins, E.B. & Tripp, T.M. 2001, *ApJS*, 137, 297.

Lazarian, A. & Visniac, E.T. 1999, *ApJ*, 517, 700.

MacLow, M., Klessen, R.S., Burkert, A., & Smith, M.D. 1998, *Phys Rev Ltr*, 80, 2754.

MacLow, M. & Klessen, R.S. 1998, *Rev Mod Phys*, 76, 125.

McKee, C.F. & Ostriker, J.P. 1977, *ApJ*, 218, 148.

Nakano, T. & Nakamura, T. 1978, *PASJ*, 30, 67.

Press, W.H., Flannery, B.P., Teukolsky, S.A., & Vetterling, W.T. 1997, *Numerical Recipes* (second edition), Cambridge University Press.

Trumpler, R.J. & Weaver, H.F. 1953, *Statistical Astronomy*, U Cal Press.

Vázquez-Semadeni, E., Gazol, A., & Scalo, J. 2000, *ApJ*, 540, 271.

Wolfire, M.G., McKee, C.F., Hollenbach, D., Tielens, A.G.G.M. 2003, *ApJ*, 587, 278.

Zweibel, E. G. 2002, *ApJ*, 567, 962.